The Pennsylvania State University

The Graduate School

Department of Energy and Mineral Engineering

MATHEMATICAL MODELING OF GEOMECHANICAL BEHAVIOR OF TARMAT DURING THE DEPLETION OF GIANT OIL RESERVOIR-AQUIFER SYSTEMS

A Thesis in

Petroleum and Mineral Engineering

by

Ayse Pamir Cirdi

Submitted in Partial Fulfillment
of the Requirements
for the Degree of

Master of Science

August 2008

The thesis of Ayse Pamir Cirdi was reviewed and approved* by the following:

Turgay Ertekin
Professor of Petroleum and Natural Gas Engineering
George E. Trimble Chair in Earth and Mineral Sciences
Graduate Program Chair
Thesis Co-Advisor

Luis Ayala
Assistant Professor of Petroleum and Natural Gas Engineering
Thesis Co-Advisor

Zuleima T. Karpyn
Assistant Professor of Petroleum and Natural Gas Engineering

*Signatures are on file in the Graduate School

ABSTRACT

Tarmat deformation and failure behavior during depletion of a giant reservoir-aquifer system is studied and a mathematical model is developed for this kind of composite systems. Deformation response of tarmat to increasing pressure differential caused by continuous depletion of reservoir is studied. In this context, geomechanical failure that takes place at the instant that the pressure differential reaches a critical value is evaluated. Fracture that occurs after this geomechanical failure is characterized. Fracture permeability that is established due to the characterized fracture is studied. Plate theory, maximum shear stress failure criterion, conventional well test model, Perkins-Kern-Nordgren model (PKN model), Khristianovic-Geertsma-de Klerk model (KGD model), flow through fractures models have been combined in a way such that tarmat behavior in giant reservoir-aquifer systems would be modeled appropriately. This sensitivity analysis, being conducted with parameters of reservoir, rock and fluid properties, proposes a protocol to find relationships and suggests designs in composite systems. The proposed methodology, ultimately, predicts fracture width and fracture permeability that would be developed in a system with a tarmat layer having a certain thickness and a reservoir being produced at a certain production rate and total depletion time.

TABLE OF CONTENTS

LIST OF FIGURES

LIST OF TABLES

ACKNOWLEDGEMENTS

I express my appreciation to Saudi Aramco, for funding this work. I emphasize my deep gratitude to my advisors Dr. Turgay Ertekin and Dr. Luis Ayala for providing me the opportunity to work in this project. During this period, their special way of guidance and support had taught me fundamental aspects of professional life, for which I am and will be grateful. I thank for Dr. Zuleima Karpyn for being in my thesis committee and part of my studies. I extend my appreciation to Dr. Derek Elsworth, Dr. Ghassan Chehab and Dr. Daniel Linzell and for spending time to guide me regarding the areas of their expertise. I thank for all faculty members that has encouraged me in this work.

I thank to my relatives, especially for *Hale Yaman*, for always being there for me. I thank for my dear friends at Penn State, at other parts of the world and at my home country. Their being there for me in every circumstance and our memories will never be forgotten. I emphasize my appreciation to dear *Ahmet Turhan*, for creating an environment in such a way that I would feel very close to my dear family back home. His guidance in my struggles, his constant support and belief in me has great contributions not only in this study but also in my happiness during two years of my life at Penn State.

I present my appreciation for my family for trusting and supporting me in every stage of my life. This work is dedicated to my heroes: My father, *Yemliha Cirdi*, my true mentor in life whom I admire more day by day, my mother, *Piraye Mujgan Cirdi*, the excellent source of balance in our lives with her loving, tolerable and understanding manner and my sister, *Yelda Meric Cirdi*, my best companion in life ever, with her mature and strong nature.

Chapter 1

Introduction

1.1 Introduction

Oil resources are located in various types of reservoir formations, varying with properties, dimensions and architectures. Creating feasible production designs with a reasonable exploration and development plan is of great importance in the production of these oil sources. The development plan requires a good understanding of not only oil and reservoir properties, but also the existing geological architecture of the reservoir of interest.

Giant oil fields, being oil sources with high production potentials, are defined as oil fields having at least 500 million barrels of ultimate recovery and they constitute almost 75% of the recoverable oil resources in the world. These fields with significant amount of recoverable oil resources, are spread into countries as Saudi Arabia, United States of America, former Soviet Union, Iran, Kuwait, Venezuela and Iraq, to name the seven largest. Saudi Arabia has known giant and potential giant reservoirs more than any other country **[Nehring, 1978].**

This study focuses on a three-layered composite system, typical of giant oil fields in the Middle East. Upper layer of the system contains the reservoir fluids, middle layer contains tarmat, and the bottom layer of the system is a high pressure water aquifer.

Middle layer, having a negligible permeability, acts like an impermeable barrier between the upper and bottom layers of the system.

The primary purpose of this study is to understand and model the behavior of the middle impermeable layer due to reservoir depletion and consequences of its behavior. Initial pressure equilibrium would be disturbed by oil production from the upper layer. This disturbance would cause a certain pressure differential between the upper and bottom boundaries of the tarmat that would eventually cause geomechanical failure of the tarmat. As a consequence of this failure, a fracture opening would occur, resulting in a certain permeability of the new system. Detailed analysis of the successive behavior of the system is of interest.

1.2 Structure of the Thesis

This thesis is composed of six chapters.

Chapter 1, titled as *Introduction* gives a general overview and description of the problem of interest. It basically explains the goal of the investigation, by mentioning the necessary outputs, their dependencies, used inputs. It also highlights a general outline of the thesis.

Chapter 2, titled as *Statement of the Problem* extends the introduction and provides a detailed description of the problem. It involves circumstantial statement of objectives of the thesis.

Chapter 3, titled as *Background Information* includes the information gathered regarding rock mechanics, oil production, plate deformation, and fracture

characterization. Failure theories and failure modes are introduced in general while the used failure theory is emphasized. Basic fundamental information on oil production is provided. Finally, approaches used to evaluate fractures and their conductivities are described.

Chapter 4, titled as *Method of Approach* provides information on how the problem is defined, approached and analyzed. It allows the reader to understand how the components of the problem definition are attached to each other in the steps of the complete analysis.

Chapter 5, titled as *Results and Discussions* gives the results of the study and includes detailed discussion regarding the obtained relationships and observed behavior.

Chapter 6, titled as *Summary*, *Conclusions and Recommended Future Work* provides the conclusions drawn from the complete study on which this thesis is based. It includes ideas about the possible ways to improve the weaknesses and/or extend the present status of the analysis.

Chapter 2

Statement of the Problem

2.1 General Description

The system under study is a composite system composed of three layers of porous medium. This composite system is depicted in **Figure 2.1** below.

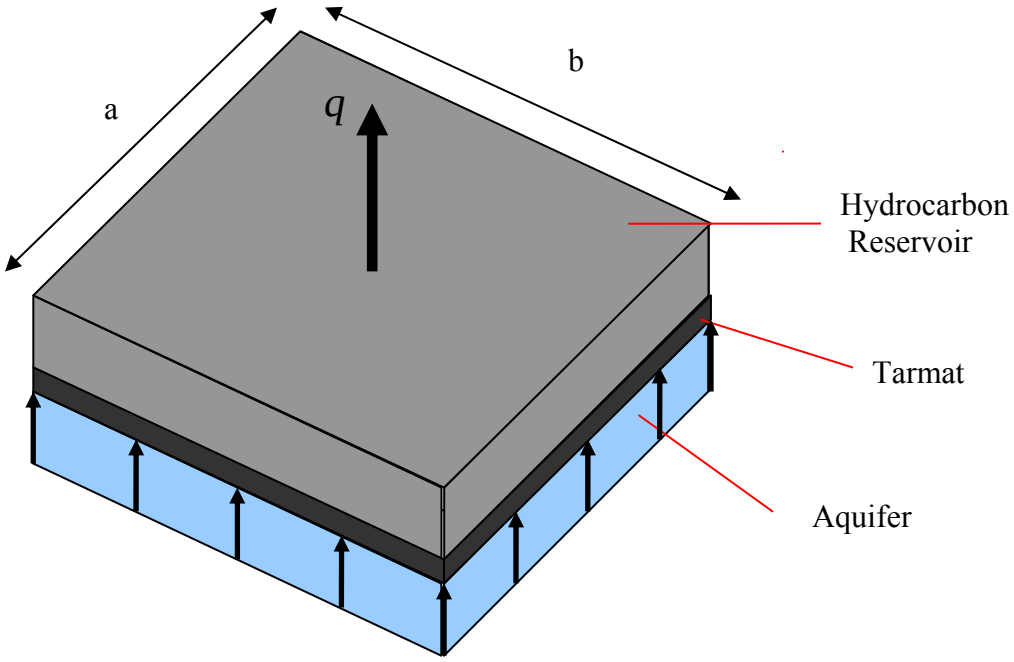

Figure 2.1: Schematic representation of the system under consideration

In **Figure 2.1**, the bottom layer is an aquifer with a strong water drive. The middle layer is a structure referred as "tarmat" with negligible permeability and the upper layer is a hydrocarbon reservoir. The tarmat is a very viscous hydrocarbon layer being composed

of tar or bitumen, which exists between oil and water contact in many cases. Having a very low permeability, it acts as a permeability barrier between the reservoir and aquifer.

Three distinct layers of the system are at the same pressure at initial conditions, before the introduction of any external disturbance to the system. As production form the hydrocarbon reservoir at the top is started, pressure at the reservoir begins to decrease gradually while pressure at the aquifer remains the same. This results in a pressure differential across the upper and bottom boundaries of the tarmat. The resulting pressure differential creates a stress filed and a deformation field. The tarmat, acting as a barrier in the middle of the system, continues to block any communication between upper layer and the bottom layer; until a critical condition of the stress field develops occur as a consequence of a certain pressure differential value. This critical condition is referred as geomechanical failure of tarmat. After the geomechanical failure, tarmat does not act as a barrier anymore and the previously created stress fields, open fractures with certain dimensions. The dimensions (i.e. width and length) of the created fracture controls the degree of communication between the hydrocarbon reservoir and the aquifer. The characterization of the fracture is of importance when evaluating the established fracture permeability.

2.2 Objectives

The main objectives of this study are two folds:

1. To characterize the geomechanical behavior of tarmat as the gradual increase of pressure differential occurs as a consequence of oil production from the

hydrocarbon reservoir. This characterization is aimed to include geomechanical failure of tarmat.

2. To evaluate the system behavior after geomachanical failure of tarmat takes place. This part of the analysis includes the fracture permeability characterization and expected communication behavior in the absence of a barrier that does not continue to act so.

In the first stage, gradual pressure differential across the upper and bottom boundaries of the tarmat and its corresponding deformation are main outputs. This analysis not only enables in finding out the pressure differential that would cause geomechanical failure, but also how much would the tarmat deform until this critical pressure differential is established.

Second stage focuses on the new form of the composite system, that follows the geomechanical failure. It is an analysis that quantifies fracture width and corresponding permeability that would be established across the fracture.

To achieve both of these objectives listed above; reservoir, rock and fluid properties are inputs of significant importance, being influencial in both of the major stages of this study.

Chapter 3

Background Information

3.1 Rock Mechanics

Rock mechanics is the area which deals with the properties of rock and the special methodology required for design of rock related components of engineering schemes **[Goodman, 1989].** Being the rock related component of the engineering design, concept of rock mechanics has major applications in common with the concept of mechanics of materials.

Mechanics of materials is the general name of the study which deals with the response of the material system to an external effect or applied disturbance **[Gere, 2001].** This study can also be referred as strength of materials and mechanics of deformable bodies.

In rock mechanics, it is very important to understand the material properties of the rock of interest, nature of the disturbance, pre-existing and present boundary conditions. Rock mechanics may come into the picture in many different engineering applications, projects and problems. In order to have a safe design in each of them, mechanical behavior should be well understood. For reliable engineering solutions, not only understanding the logical developments of rock mechanics principles is necessary, but also is the correct application of these solutions to the practical and appropriate situations. To do this; stresses, strains and displacement of structures due to the applied load that is

acting on them should be determined. In other words, in order to have a complete picture of mechanical behavior of rocks, stresses, strains and deformations due to prevailing loading condition at a specific time should be evaluated until failure conditions are reached. This study requires a relevant failure criterion selection depending on the problem of interest.

3.1.1 Concept of Stress and Strain

Concept of stress and strain should be well understood to be able to evaluate the rock behavior mainly controlled by the nature of disturbance and rock properties **[Whittaker *et al.*, 1992, Gere, 2001].** Before defining rock properties which are significant parameters in the analysis presented in this thesis, stress, strain and their relations are reviewed in the rest of this part of the current section.

Stresses are classified as, normal stresses and shear stresses. Strain associated with normal stress is referred as normal strain where strain associated with shear stress is shear strain. Relationship between stress and strain is important to understand the behavior of material of interest. To obtain this relationship for particular materials; tension and compression tests can be performed. These tests are performed at different magnitudes of the applied load. The diagram, which shows stress and strain relationship by plotting obtained results as stress versus strain is called stress-strain diagram. A typical stress-strain diagram for a particular material can be observed in **Figure 3.1.** Elastic behaving and plastic behaving regions are marked. If the material is beyond the elastic behaving region, it would not behave similarly when unloaded. However, if it

stays in the elastic beviour region, it can behave similarly no matter the number of loading cyles and types.

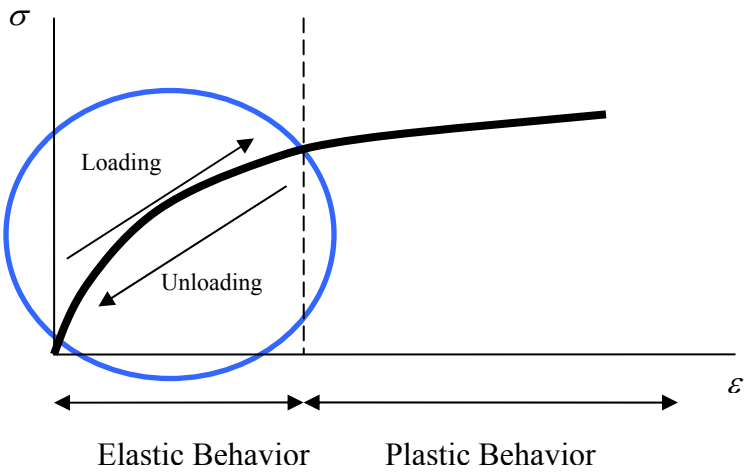

Figure 3.1: Stress-strain diagram showing elastic and plastic regions

Normal stress occurs as an object is axially loaded by a force with a certain magnitude and direction. Uniformly distributed normal stress that occurs due to this type of loading is indicated by **Equation 3.1.** Note that this is a uniformly disributed stress.

$$\sigma = \frac{P}{A} \qquad \textbf{(Eq. 3.1)}$$

In **Equation 3.1**; σ is normal stress, P is axial force and A is cross sectional area.

In cases where tensile forces are being applied to the object, normal stress is tensile and in cases where compressive forces are being applied to the object, normal stress is compressive. In the case of tensile stress, object elongates while in the case of compressive stress, object shortens. Elongation or contraction per unit length is defined as strain and expressed by **Equation 3.2;**

$$\varepsilon = \frac{\delta}{L} \qquad \textbf{(Eq. 3.2)}$$

In **Equation 3.2**; ε is normal strain, δ is elongation or contraction and L is original length.

Shear stress occurs as an object is tangentially loaded by a force with a certain magnitude and direction. Shear stresses that occur due to this type of loading is indicated by **Equation 3.3;**

$$\tau = \frac{V}{A} \qquad \textbf{(Eq. 3.3)}$$

In **Equation 3.3**; τ is shear stress, V is shear force and A is cross sectional area.

Shear strains are defined as shape changing factors rather than causing elongations or contractions. Angles between the side faces of the elements that are subjected to shear stress, change.

Another important concept about stress is, principle stresses. These stresses are defined as maximum and minimum normal stresses. Principle stresses are associated not only with normal stresses, but also with shear stresses. **Equation 3.4** expresses the relation of principle plane angle, normal stresses and shear stress, while its geometric representation is denoted by **Figure 3.2.**

$$\tan 2\theta_p = \frac{2\tau_{xy}}{\sigma_x - \sigma_y} \qquad \textbf{(Eq. 3.4)}$$

In **Equation 3.4**; θ_p is principle angle, τ_{xy} is shear stress, σ_x is normal stress in x direction, σ_y is normal stress in y direction.

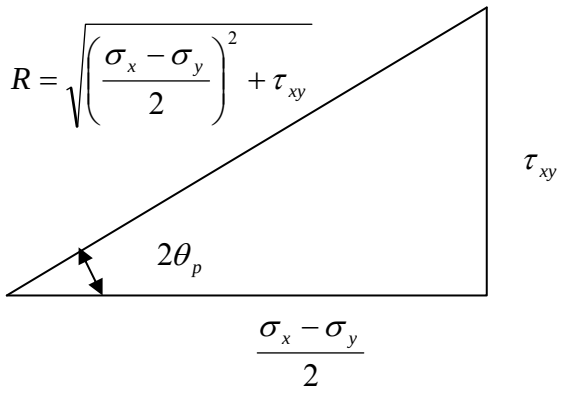

Figure 3.2: Geometric representation of **Equation 3.4**

General expression for first and second principle stresses is given by **Equation 3.5** and is based on sum of normal stresses on perpendicular planes being equal.

$$\sigma_{1,2} = \frac{\sigma_x + \sigma_y}{2} \pm \sqrt{\left(\frac{\sigma_x - \sigma_y}{2}\right)^2 + \tau_{xy}{}^2} \qquad \textbf{(Eq. 3.5)}$$

In **Equation 3.5;** $\sigma_{1,2}$ is first and second principle stresses, respectively shown by subscripts. On the other hand, the third principle stress, σ_3 may be larger or smaller than the other two principle stresses. In two dimensional analyses it is assumed to be zero.

3.1.2 Properties of Rocks

Material properties of the rocks is an influencial aspect of rock mechanics. Their effect can be observed in the complete picture of each of the specific rock mechanics problems.

Influencial geomechanical rock properties that come into the picture in the specific problem studied in this work are Young's modulus of elasticity, Poisson's ratio and strength.

Young's modulus of elasticity is a constant of proportionality that is a function of axial stress and the axial strain. Their relationship is expressed by the **Equation 3.6;**

$$E = \frac{\sigma}{\varepsilon} \qquad \textbf{(Eq. 3.6)}$$

In **Equation 3.6;** E is Young's modulus of elasticity, σ is axial stress and ε is axial strain.

Equation 3.6 is a form of Hooke's Law, which has been solved for Young's modulus of elasticity. Hooke's Law is denoted by **Equation 3.7;**

$$\sigma = E\varepsilon \qquad \textbf{(Eq. 3.7)}$$

This property can be obtained from a stress-strain diagram of a linearly elastic material or from the linear elastic portion of the stress strain diagram of a material, which is basically the slope. Linearly elastic materials show a linear relationship between stress and strain as well as behaving elastically **[Gere, 2001].**

Poisson's ratio, which represents a dimensionless quantity, is a property that relates lateral strain and axial strain. This relationsip is a necessary material property since a material in tension encounters not only an axial elongation but also a lateral contraction. The lateral strain at any point in the material that is in tension is directly proportional to the axial strain at the same point. This is valid for linearly elastic materials. Following expression in **Equation 3.8** is the definition of Poisson's ratio that is function of lateral strain and axial strain:

$$\nu = -\frac{\varepsilon'}{\varepsilon} \qquad \textbf{(Eq. 3.8)}$$

In **Equation 3.8**; ν is Poisson's ratio, ε' is lateral strain and ε is axial strain. Presence of a minus sign is due to the fact that lateral strain and axial strain has opposite signs **[Gere, 2001].**

One of the most important rock properties is its strength. There are different types of rock strength, mainly compressive strength, tensile strength and yield strength **[Toulokian *et al.*, 1981].** There is a dominating strength that effects conclusions of a specific study, due to the problem definition.

There are testing methods to determine strength of rock masses in which the representative rock specimen is taken to apply the test of interest. Strength testing methods that are in extensive usage are unconfined compression tests, confined compression tests, shear tests, direct tension tests and indirect tension tests.

Unconfined compression test is a method to determine compressive strength of the rock sample being tested. This method has a complex procedure and results are dependent on how the procedure is applied. Rock specimen that is in common usage in that type of testing method is cylindrical and its length to width ratio is in between 2 and 2.5. Flat, smooth and parallel ends of the cylinder is cut perpendicularly to the axis of the cylinder. There are various applications to smoothen the ends or reducing the friction. Following expression, **Equation 3.9** shows how the compressive srength is determined due to applied load to the rock cylinder with a certain cross section:

$$q_u = \frac{P}{A} \qquad \textbf{(Eq. 3.9)}$$

In **Equation 3.9**; q_u is compressive strength, P is peak load and A is cross sectional area **[Goodman, 1989].**

Triaxial compression test is a method to determine compressive strength of the rock. In this procedure cylindirically shaped rock sample is compressed and confining pressure is applied to it at the same time. At the peak load, following conditions occur which are expressed by **Equation 3.10** and **Equation 3.11** as shown below.

$$\sigma_1 = \frac{P}{A} \qquad \textbf{(Eq. 3.10)}$$

$$\sigma_3 = P' \qquad \textbf{(Eq. 3.11)}$$

In **Equation 3.10** and **Equation 3.11**; P is peak load (highest load supportable parallel to the axis of the cylinder), σ_1 is first principle stress, σ_3 is third principle stress, P' is pressure in the confining medium and A is cross sectional area of the rock cylinder.

As a result of application of confining pressure, confinement effect, that is the strengthening of the rock sample, occurs. This effect is significantly observed in many rock types. In a regular triaxial compression test, first step is to apply P' as it surrounds the cylinder. This causes first and third principle stresses to be equal to the confining pressure. Following step is the application of $\sigma_1 - P'$ as an axial load, while the lateral pressure is not changing **[Goodman, 1989].**

Brazillian test, or *splitting tensile test*, is a method to determine the tensile strength of the rock. The Brazillian test is applied for cylindirical concrete specimens by loading them on their side in a compression machine. As a result of this type of loading,

rock core splits along the diameter and parallel to the cylindirical axis. Crack is almost as long as the diameter. Tensile strength is estimated by **Equation 3.12** below:

$$\sigma_{t,B} = \frac{2P}{\pi dt} \qquad \textbf{(Eq. 3.12)}$$

In **Equation 3.12;** $\sigma_{t,B}$ is estimated tensile strength, P is peak compression load, d is diameter of the cylinder and t is thickness of the disk or length of the cylinder.

It should be noted that tensile strength estimate in Brazilian test is quite different from that in the direct tension test. This difference varies from case to case. This happens due to the fact that fissures are also effecting the failure in Brazilion test procedure, on top of the tensile stress **[Goodman, 1989, Toulokian *et al*., 1981].**

Flexural test is a method to determine failure point of a rock by bending. It is based on simple beam theory where beam bending occurs at perfectly elastic conditions. A representative rock beam is used in this method. It is supported from both of its ends and loads are applied from $L/3$ distance from each edge. Determined strength is the tensile stress of the rock beam which corresponds to the peak load applied to the beam. Peak tensile stress here is referred as modulus of rupture or flexural strength. Flexural strength mostly corresponds to the double or tripple of the actual tensile strength. **Equation 3.13** gives the expression for modulus of rupture:

$$T_{MR} = \frac{16PL}{3\pi d^3} \qquad \textbf{(Eq. 3.13)}$$

In **Equation 3.13**; T_{MR} is modulus of rupture, P is peak load, L is length between load reactions on the lower surface and d is diameter of the core **[Goodman, 1989].**

Ring shear test is a method to determine strength of the intact rock in terms of confining pressure. Specimen used in this testing method may or may not have square and smooth ends. Load is applied parallel to the axis of the core specimen. The application of load to the plunger causes shear to occur on two planes. This leads formation of two fracture surfaces along the planes. Due to the results, strength increases with confining pressure. Relation of peak load on the plunger, cross sectional area of the core sample and shear strength of the intact rock is expressed in **Equation 3.14:**

$$\tau_p = \frac{P}{2A} \qquad \textbf{(Eq. 3.14)}$$

In **Equation 3.14;** τ_p is peak shear stress, i.e. shear strength, P is peak load applied to the plunger and A is cross sectional area of the core sample **[Goodman, 1989].**

3.1.3 Failure Theories and Failure Modes

3.1.3.1 Failure Theories

Maximum shear stress failure criterion is based on the theory that is suggested by Charles Coulomb **(1773)** and Henry Tresca **(1868).** Due to this theory, failure point is reached when the maximum shear stress in the material becomes equal to the value of the shear stress at yielding. This point, which indicates the occurance of failure is referred as yield strength and can be determined by uniaxial compression or uniaxial tension test. In **Figure 3.3**, uniaxial specimen that is subjected to σ_0 as a tensile stress and related Mohr's circle can be seen.

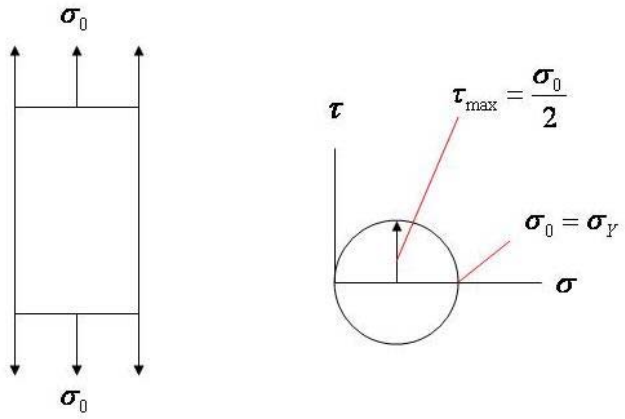

Figure 3.3: Uniaxial specimen subjected to a tensile stress and its related Mohr's circle

As can be observed, $\sigma_0 = \sigma_Y$, while the maximum shear stress is given in **Equation 3.15:**

$$\tau_{max} = \tau_Y = \frac{\sigma_o}{2} \qquad \textbf{(Eq. 3.15)}$$

This equation denotes the situation that the failure point is reached, by expressing maximum shear stress, τ_{max}, being equal to the shear stress at yield, τ_Y. For instance, if principle stresses are ordered as σ_3, σ_2 and σ_1, respectively in terms of magnitude in a case; maximum shear stress and the condition when the failure occurs are given by **Equation 3.16** and **Equation 3.17,** respectively:

$$\tau_{max} = \frac{\sigma_1 - \sigma_3}{2} \qquad \textbf{(Eq. 3.16)}$$

$$\frac{\sigma_1 - \sigma_3}{2} = \tau_Y = \frac{\sigma_Y}{2} \qquad \textbf{(Eq. 3.17)}$$

Previous case or similar ones with different magnitude orders of principle stresses may not always be cases to be encountered. In some cases, one of the principle stresses may be zero while the other two are not. There are three main combinations of these type of cases in which σ_3 is selected to be the one that is equal to zero. First case which may occur is $\sigma_1 \rangle \sigma_2 \rangle 0$, $\sigma_3 = 0$. The block with principle stresses acting on it, τ_{max} plane of the block and related Mohr's circle, with stress relations is given in **Figure 3.4.**

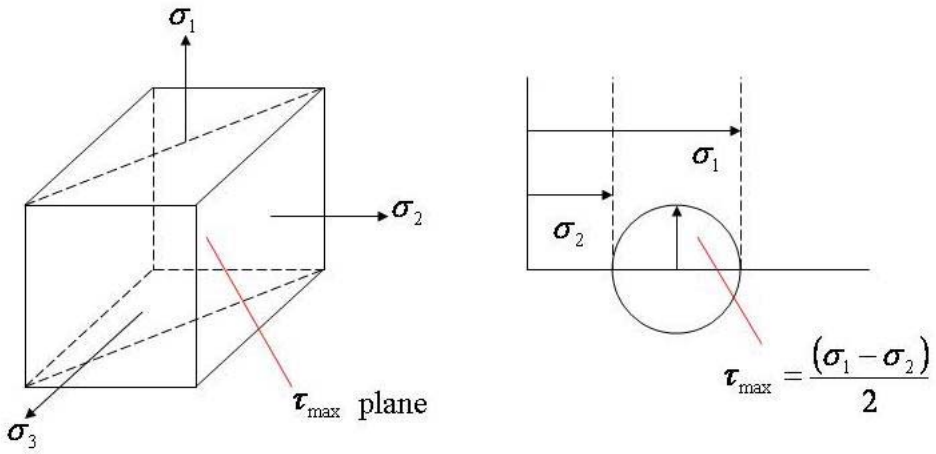

Figure 3.4: Maximum shear stresses for $\sigma_1 \rangle \sigma_2 \rangle 0$, $\sigma_3 = 0$

It can be deduced that $\frac{(\sigma_1 - 0)}{2} \rangle \frac{(\sigma_1 - \sigma_2)}{2}$ from the figure denoting this case. In conclusion, absolute maximum shear stress of this case is given in **Equation 3.18:**

$$\tau_{max} = \frac{\sigma_1}{2} \qquad \textbf{(Eq. 3.18)}$$

Second case which may occur is $\sigma_2 \langle \sigma_1 \langle 0$, $\sigma_3 = 0$. The block with principle stresses acting on it, τ_{max} plane of the block and related Mohr's circle, with stress relations is given in **Figure 3.5.**

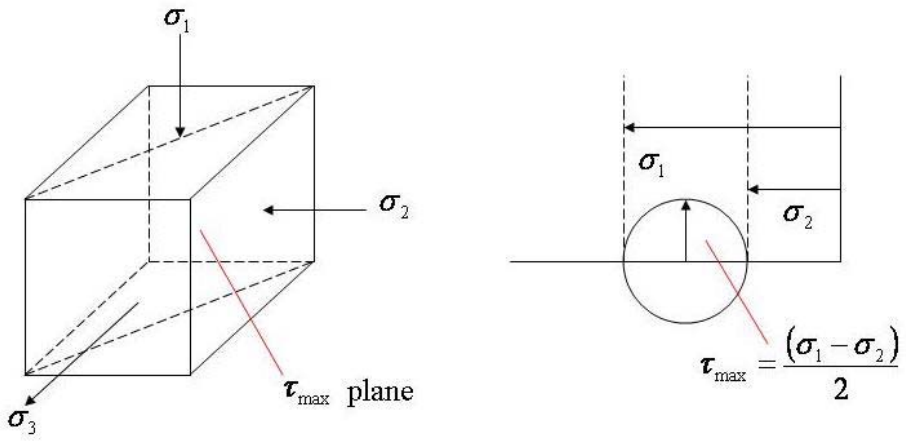

Figure 3.5: Maximum shear stresses for $\sigma_2 \langle \sigma_1 \langle 0$, $\sigma_3 = 0$

Again, it can be deduced that $\frac{|\sigma_2 - 0|}{2} \rangle \frac{(\sigma_1 - \sigma_2)}{2}$ from the figure denoting this case. In conclusion, absolute maximum shear stress of this case is given in **Equation 3.19:**

$$\tau_{max} = \frac{|\sigma_2|}{2} \qquad \textbf{(Eq. 3.19)}$$

Third case which may occur is $\sigma_1 \rangle 0$, $\sigma_2 \langle 0$, $\sigma_3 = 0$. The block with principle stresses acting on it, τ_{max} plane of the block and related Mohr's circle, with stress relations is given in **Figure 3.6**.

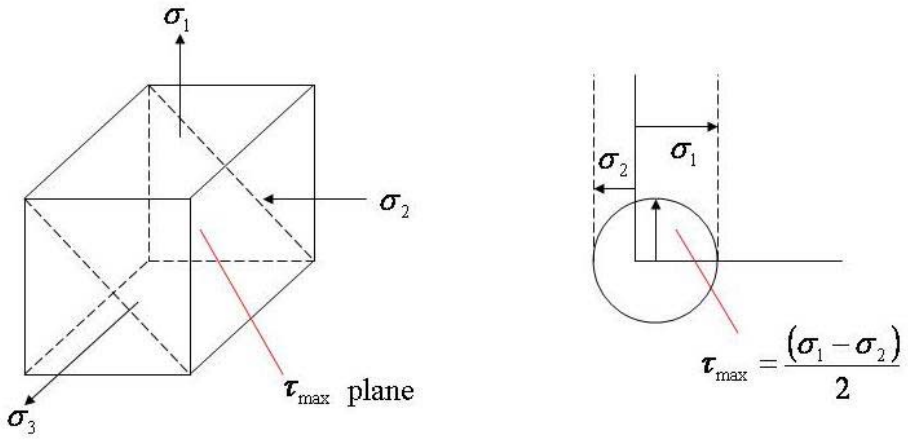

Figure 3.6: Maximum shear stresses for $\sigma_1 \rangle 0$, $\sigma_2 \langle 0$, $\sigma_3 = 0$

Similarly, it can be deduced that $\frac{(\sigma_1 - \sigma_2)}{2} \rangle \frac{\sigma_1}{2}$ and $\frac{(\sigma_1 - \sigma_2)}{2} \rangle \frac{|\sigma_2|}{2}$ from the figure denoting this case. In conclusion, absolute maximum shear stress of this case is given by **Equation 3.20:**

$$\tau_{max} = \frac{\sigma_1 - \sigma_2}{2} \qquad \textbf{(Eq. 3.20)}$$

For the cases above, in which σ_3 is equal to zero, maximum shear stress can be denoted by **Equation 3.21** as:

$$\tau_{max} = \max\left(\left|\frac{\sigma_1}{2}\right|, \left|\frac{\sigma_2}{2}\right|, \left|\frac{\sigma_1 - \sigma_2}{2}\right|\right) \qquad \textbf{(Eq. 3.21)}$$

This equation summarizes all possible cases and their related maximum shear stresses. Failure occurs if the any of the above values becomes equal to or exceeds the allowable shear stress; $\frac{\sigma_Y}{2}$ **[Bickford, 1998].**

Mohr-Coulomb failure criterion is a common way of evaluating failure by relating shearing resistance to contact forces, friction and cohesion that is present among the rock grains. **Equation 3.22** gives the following relation:

$$\tau = C + \sigma_n^{'} \tan\phi \qquad \textbf{(Eq. 3.22)}$$

In **Equation 3.22**; τ is shear stress, C is cohesive strength, ϕ is angle of internal friction or friction angle and $\sigma_n^{'}$ is effective normal stress acting on the grains.

A linear relationship exists between τ and $\sigma_n^{'}$. C and ϕ are linearization factors. This criterion is evaluating failure when failure occurs due to shear forces becoming dominant. If this criterion is used for inappropriate cases, deviation from this linearity is observed. Construction of failure envelopes can be achieved by using a number of Mohr's circles. Each circle represents a triaxial test in which $\sigma_2 = \sigma_3$ and σ_1, axial stress, is being increased until failure is observed. Once the envelope is constructed, it can be treated as a separating border of safe zone and failed zone. Failure envelope may be expressed in terms of σ_1 and σ_3. **Equation 3.23**, **Equation 3.24** and **Equation 3.25** represent this analysis:

$$\sigma_1^{'} = \frac{1+\sin\phi}{1-\sin\phi}\sigma_3^{'} + C_0 \qquad \textbf{(Eq. 3.23)}$$

$$C_0 = 2C\tan\left(\frac{\pi}{4}+\frac{\phi}{2}\right) = 2C\frac{\cos\phi}{1-\sin\phi} \qquad \textbf{(Eq. 3.24)}$$

$$\sigma_1^{'} = C_0 + \sigma_3^{'}\tan^2\left(\frac{\pi}{4}+\frac{\phi}{2}\right) \qquad \textbf{(Eq. 3.25)}$$

After constructing failure envelope, normal stresses and shear stresses may be calculated by assuming internal friction angle to be 45^0. **Equation 3.26** and **Equation 3.27** below can be evaluated for finding points to use in the stability analysis:

$$\sigma_n^{'} = \frac{\sigma_1+\sigma_3}{2} - \alpha P_r \qquad \textbf{(Eq. 3.26)}$$

$$\tau_{\max} = \frac{\sigma_1-\sigma_2}{2} \qquad \textbf{(Eq. 3.27)}$$

These two points can be plotted on the figure and checked for stability **[Fjaher *et al.*,1992, Lianyang, 2005, Economides *et al.*, 1998].**

Internal friction theory or *Coulomb-Mohr failure criterion* is appropriate to be applied for brittle materials. It is based on condition of principle stresses and ultimate tensile and ultimate compressive strengths of the material of interest. Ultimate tensile strength and ultimate compressive strength are material dependent properties and they can be determined by uniaxial tension and uniaxial compression tests, respectively. Internal friction theory can be well explained by **Figure 3.7.**

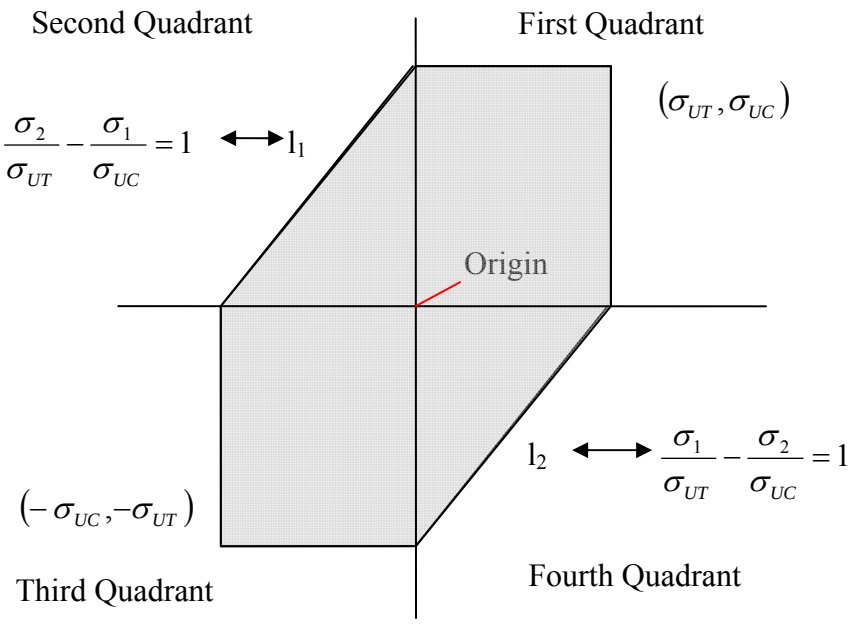

Figure 3.7: Safe regions and their relevant equations for internal friction theory

As can be seen in **Figure 3.7,** squares in the first and third quadrants are safe regions, in which failure is not observed. In these squares, principle stresses are both positive or both negative. However, the second and fourth quadrants are the quadrants when principle stresses have opposite signs with each other. Safe regions are determined by lines l_1 and l_2 for this case. Equations which represent l_1 and l_2 in terms of principle stresses and ultimate tensile and compressive strengths are expressed by **Equation 3.28** and **Equation 3.29,** respectively:

$$\frac{\sigma_2}{\sigma_{UT}} - \frac{\sigma_1}{\sigma_{UC}} = 1 \qquad \textbf{(Eq. 3.28)}$$

$$\frac{\sigma_1}{\sigma_{UT}} - \frac{\sigma_2}{\sigma_{UC}} = 1 \qquad \textbf{(Eq. 3.29)}$$

Due to this theory, failure occurs if any state of principle stresses lie outside the shaded region **[Bickford, 1998].**

Maximum normal stress failure criterion is another criterion that is suitable for failure prediction of brittle materials. It is based on maximum principle stress reaching ultimate normal stress value of the material of interest. This criterion would give reasonable conclusions only if the tensile principle stress has a comparable magnitude with the ultimate normal stress. Ultimate normal stress; σ_{ULT} is determined by uniaxial tension test. Due to this criterion, if any combination of $\left(\frac{\sigma_1}{\sigma_{ULT}}, \frac{\sigma_2}{\sigma_{ULT}}\right)$ is outside the closed region of a unit square that has corners (1,1), (-1,1), (-1,-1), (1,-1) in four quadrants, this indicates failure **[Bickford, 1998].**

Hoek-Brown failure criterion is an empirical approach to evaluate failure. It suggests a reasonable range when the failure taking place is brittle. It may lead to poor results when ductile failure is of interest. This criterion is common in applications when naturally fractured reservoirs are of interest. Empirical formulation is expressed in **Equation 3.30** below:

$$\sigma_1^{'} = \sigma_3^{'} + \sqrt{(I_m C_0 \sigma_3 + I_S C_0^2)} \qquad \textbf{(Eq. 3.30)}$$

I_m and I_S are frictional index and intact index respectively. They are material properties. Together with C_O, these material properties are measured in laboratories [**Economides *et al.*, 1998].**

Von Mises failure criterion is an appropriate criterion for the materials which would be classified as ductile. This theory is identical to the criterion suggested by

octahedral shear stress theory. Due to this theory, failure is predicted to be the point at which octahedral shear stress becomes equal to the value of the octahedral stress at yielding in a uniaxial tensile test. Principle planes and octahedral planes are shown in **Figure 3.8.**

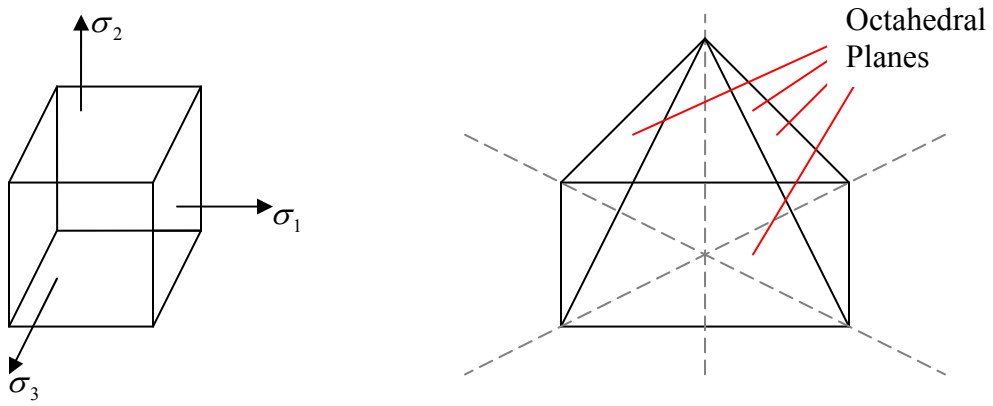

Figure 3.8: Principle planes and octahedral planes

Normal stress and shear stress that is acting on each octahedral plane is expressed by **Equation 3.31** and **Equation 3.32,** respectively:

$$\sigma_{oct} = \frac{(\sigma_1 + \sigma_2 + \sigma_3)}{3} \qquad \textbf{(Eq. 3.31)}$$

$$\tau_{oct} = \frac{1}{2}\sqrt{(\sigma_1 - \sigma_2)^2 + (\sigma_2 - \sigma_3)^2 + (\sigma_3 - \sigma_1)^2} \qquad \textbf{(Eq. 3.32)}$$

In an uniaxial tensile test, σ_1 is equal to yield stress, σ_Y, while σ_2 and σ_3 are both equal to zero. After making these substitutions to **Equation 3.32**, **Equation 3.33** below can be obtained:

$$\tau_{oct} = \frac{1}{2}\sqrt{(\sigma_Y - 0)^2 + (0 - 0)^2 + (0 - \sigma_Y)^2} = \frac{\sigma_Y}{\sqrt{2}} \qquad \textbf{(Eq. 3.33)}$$

Equation 3.34 can be obtained after solving **Equation 3.32** and **Equation 3.33** together for σ_Y and it gives the criterion for failure in terms of principle stresses and yield stress **[Bickford, 1998].**

$$\sigma_Y = \frac{1}{\sqrt{2}}\sqrt{(\sigma_1 - \sigma_2)^2 + (\sigma_2 - \sigma_3)^2 + (\sigma_3 - \sigma_1)^2} \qquad \textbf{(Eq. 3.34)}$$

Drucker-Prager criterion is an extended version of Von Mises failure criterion. It is based on **Equation 3.35** as shown below:

$$\alpha I_1 + \sqrt{J_2} - K = 0 \qquad \textbf{(Eq. 3.35)}$$

In **Equation 3.35;** K and α are material properties which are functions of internal friction angle; ϕ and cohesion; C. I_1 and J_2 are functions of effective principle stresses. Failure point is evaluated when $\sqrt{J_2}$ versus I_1 is plotted **[Economides *et al.*, 1998].**

Griffith Crack theory is a theory that may be applied to rock fracture. This theory is applicable to elastic materials. It gives reasonable results when brittle failure occurs. There are extended versions of this theory which deals with fluid pressure failure **[Toulokian *et al*., 1981].**

3.1.3.2 Failure Modes

There exists various possible dominating failure modes depending mainly on the applied loading configuration of the load carrying rock. They can be categorized as;

failure due to flexure, failure due to bending, failure due to tension and failure due to compression. More than one certain failure mode can be the most recognised mode due to the case of interest.

Failure due to flexure occurs due to the bending of the rock. The bending of interest of the rock is supported and accelarated by occurance of tensile cracks. This type of failure basically occurs due to the occurance of disconnection between original rock and the roof on it. As a consequence, a gap forms and rock beam bends downward due to the gravitational effect, ending up with cracks. Layers above a mine roof is a typical example for this type of failure.

Failure due to shear occurs as the shear stress approaches to a critical value. That is, a surface of rupture is created due to critical shear stresses. If shear stresses are released to the critical value as displacement occurs throughout the rupture surface, shear failure occurs. Typically, shear failure is encountered by fault zones, weathered or/and crushed rock structures, slopes having soil like rocks or weak zones.

Failure due to direct tension occurs in rock layers that are oriented convex upward. Surface of rupture that occurs due to this type of failure is free from the wheathered rock particles. Basically, even if the friction would not allow the base of the rock to be steep, the inner layer has inclinations steeper than frictional allowance. Stable part of the rock applies a tensile force and pulls form the above part of the slope.

Failure due to direct compression occurs due to the formation of small particles at the compression zone. They occur due to cracking. They stay attached to the compression zone and end up with crushing. This type of failure is also called as crushing failure. It is

common in shortened rock volumes and penetrated rocks. Rocks under drilling bits, or cutters of boring machines are some common examples **[Goodman, 1989].**

3.2 Oil Production and Well Testing

Estimation of the capacity and performance of wells under production is important. In order to have such an estimate, well tests are implemented. These tests are mainly categorized as pressure build up tests and flow tests. Each of these tests helps characterizing various formation properties. Build up tests are ideal build up test, actual build up test and reservoir limits test and flow tests are drawdown tests and multirate tests.

In order to estimate the pressure behavior of a case in which a drainage area with a single well is of interest, shape factors for the conventional well test model can be used. These shape factors include many drainage area shapes and possible well locations. Evaluations at any observation point located in the drainage area of interest, is possible to make. Tables regarding this analysis are present in the literature. In this analysis influential parameters are reservoir and fluid properties, reservoir dimensions and production rate of the well. Reservoir and fluid properties are porosity, permeability, thickness, compressibility, viscosity, formation volume factor and initial pressure. Wellbore radius is also influential in this type of analyses **[Lee, 1982].**

3.3 Plate Theory

Plate theory is a fundamental theory, that is encountered in many engineering applications. In addition to basics of this theory, there are specific studies related to plate theory, in literature **[Bickford, 1998, Boresi and Schmidt, 2003, Timoshenko and Woinowski-Krieger, 1959].**

Flat surfaces which are used to support loads that are perpendicular to their surface are called plates or flat plates. Geometry of a flat plane is defined such that there exists a $z = 0$ plane that lies within the plate. The $z = 0$ plane is called the middle surface of the plate, since it is assumed that material of the plate lies symmetrically about $z = 0$ plane. Dimension that is perpendicular to vertical axis is the thickness of the plate. It is denoted by h. Flat plates have lateral dimensions or radial dimensions, depending on their shape. They have various types of supporting and loading conditions.

Figure 3.9 shows a plate with its middle surface, supports and loading in general. From many shapes that a plate may have, a rectangular shaped plate is displayed here. Other possible plate shapes are circular and annular plates.

In a similar fashion that is observed in beams, internal forces occur as the flat plate resists the transverse loading that is being applied to it. **Figure 3.10** shows a flat plate in which loading, original shape and deformed shape can be observed. Again, a rectangular shaped plate is displayed here. Loading that is applied to the plate maybe uniform or non-uniform.

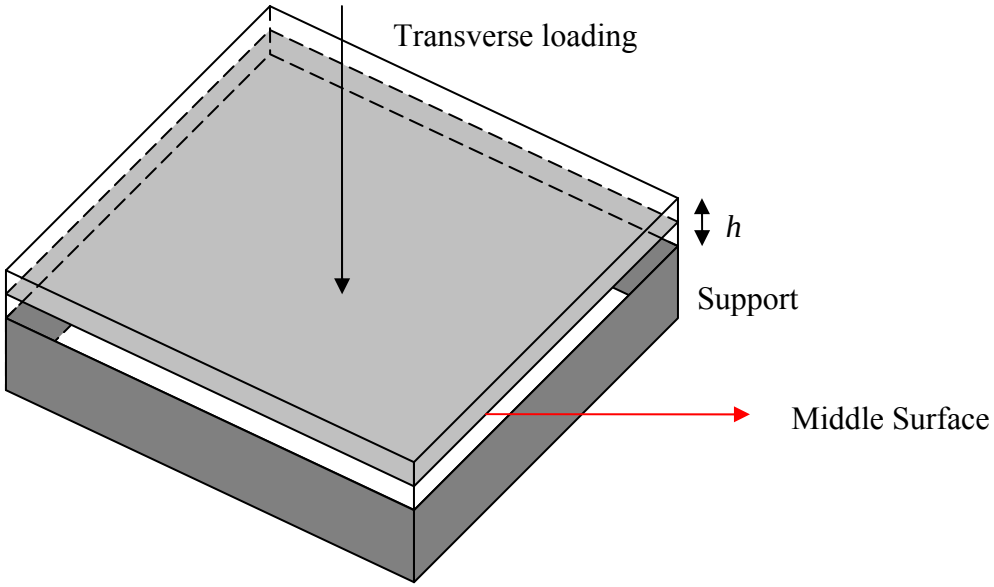

Figure 3.9: Geometry of a flat plate (case of a rectangular plate)

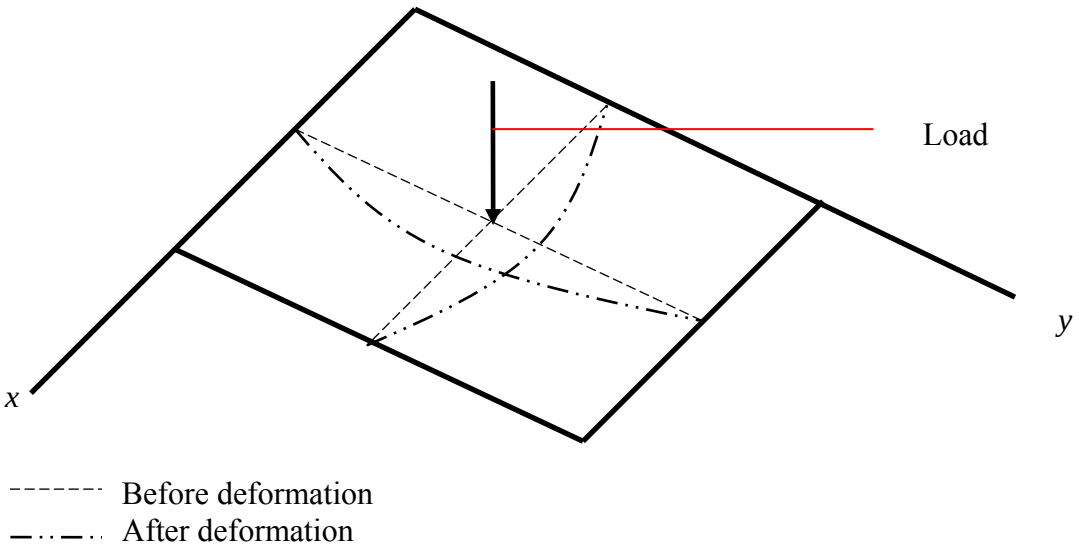

Figure 3.10: Deformation and loading on a flat plate (case of a rectangular plate)

In plate analysis, boundary conditions are very significant. Possible boundary conditions are simply supported edges, clamped edges and free edges. These boundary conditions may exist in both circular and rectangular plates. Coupled forms of different boundary conditions may exist in some cases. **Figure 3.11** and **Figure 3.12** display simply supported and clamped boundary conditions respectively. Equations that are placed in these figures are explained in Chapter 4 in detail.

Edges 1 and 3:

$$w = 0$$

$$M_y = D\left(\frac{\partial^2 w}{\partial y^2} + \nu\frac{\partial^2 w}{\partial x^2}\right) = 0$$

Edges 2 and 4:

$$w = 0$$

$$M_x = D\left(\frac{\partial^2 w}{\partial x^2} + \nu\frac{\partial^2 w}{\partial y^2}\right) = 0$$

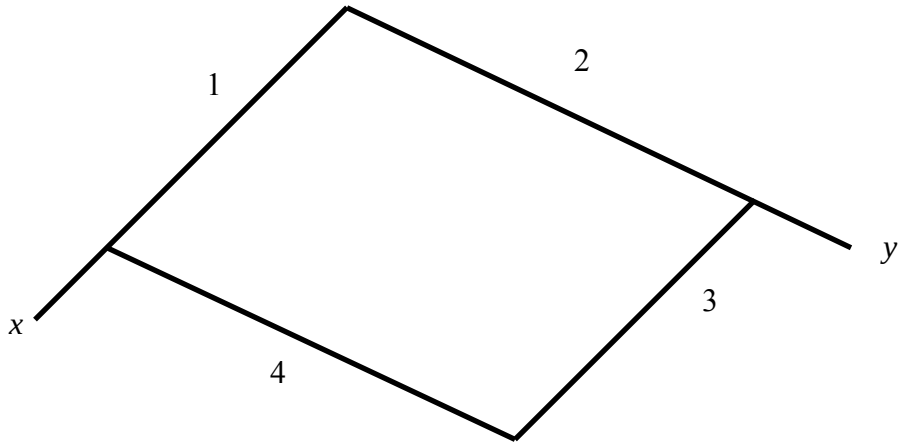

Figure 3.11: Boundary conditions for simply supported edges (all edges)

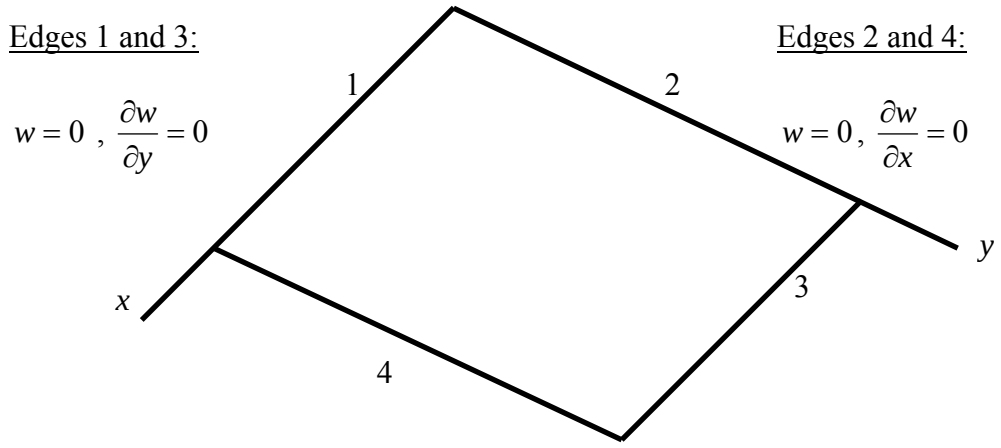

Figure 3.12: Boundary conditions for clamped edges (all edges)

3.4 Hydraulic Fracturing Models and Fracture Width Characterization

Fractures can occur naturally or can be artificially created. Natural fractures occur depending on the geomechanical properties of rock of interest and nature of external disturbances. Artificially created fractures also depend on geomechanical properties of rock of interest, accompanied by design parameters. Hydraulic fracturing is a method to create fractures that would not occur naturally.

Main reason of this artificial process is increasing possible production of oil and gas. This process involves injection of a fluid into certain wellbore section. Injection is done at a high pressure with a reasonable fracturing fluid selection. Created fracture reaches the section that is believed to contain oil or gas **[Yew, 1997].**

Apart from improving productivity, hydraulic fracturing is also useful in overcoming wellbore damage, contributing in secondary recovery operations and helping injection of brine and waste material **[Howard and Fast, 1970].**

In order to design successful hydraulic fracturing operations, dimensions and propagation characteristics of the fracture of interest should be taken into account thoroughly. In literature, there are models which enable a good understanding of relationships of influential parameters in this concept. Among these hydraulic fracturing models, Perkins-Kern-Nordgren model (PKN model) and Khristianovic-Geertsma-de Klerk model (KGD model) are helpful in determining fracture width. Average fracture width may be calculated as a function of injection rate, viscosity and specific gravity of the fracturing fluid, Poisson's ratio, Young's modulus of elasticity and shear modulus, of the rock that is composing fractured formation, thickness and length of the fracture. Shear modulus of the rock is a function of Poisson's ratio and Young's modulus of elasticity.

Expressions giving width calculations by PKN model and KGD model are given in **Equation 3.36** and **Equation 3.37,** respectively:

$$w = 0.3\left[\frac{q_i \mu(1-\nu)x_f}{G}\right]^{1/4}\left(\frac{\pi}{4}\gamma\right) \qquad \textbf{(Eq. 3.36)}$$

$$w = 0.29\left[\frac{q_i \mu(1-\nu)x_f^2}{Gh_f}\right]^{1/4}\left(\frac{\pi}{4}\right) \qquad \textbf{(Eq. 3.37)}$$

In **Equation 3.36** and **Equation 3.37**; w is fracture width (in), q_i is injection rate (BPM/d), μ is fluid viscosity (cp), ν is Poisson's ratio, x_f is half fracture length (ft), G is shear modulus (psi), γ is specific gravity of the fluid **[Economides, 1992].**

3.5 Fracture Permeability Models

In general, permeability is a rock property which corresponds to rocks ability to allow transmission of any fluid through its structure. Any rock is permeable and usually contains water or moisture in pore spaces or/and any discontinuities of it **[Goodman, 1989].**

Fractured rocks, natural or artificial, contribute the increase in rocks' fluid flow capacity, by increasing their permeability. Fracture's fluid carrying capacity is strongly dependent on its width. Among literature, there are models focusing on fracture width analysis and relating fracture permeability to fracture width. One of these models is referred as viscous flow of wetting fluids through smooth fractures of constant width **[Craft and Hawkins, 1959].** This model both deals with fracture width analysis and relates permeability to fracture width. Second one is referred as flow of hydraulic fracturing fluids through the induced fractures **[Yew, 1997].** This model is focused on fracture width analysis. However, it is possible to relate fracture permeability to fracture width with the help of this model.

Modelling of viscous flow of wetting fluids through smooth fractures of constrant width is very similar to Poiseulle's law for capillary flow, except for the shape of the void space that the fluid flows through.

Flow equation obtained for this model is given by **Equation 3.38.** Its derivation is provided in detail in Chapter 4 of this thesis.

$$q = \frac{w^2 A(P_1 - P_2)}{12\mu L} \qquad \textbf{(Eq. 3.38)}$$

In **Equation 3.38;** q is volumetric flow rate, w is width of the fracture, A is cross sectional area of the fracture, $(P_1 - P_2)$ is pressure differential between the ends of the fracture, μ is viscosity of the flowing fluid and L is fracture length.

Combining **Equation 3.38** with Darcy's law expressed in similar units, permeability term is expressed in terms of width. **Equation 3.39** denotes this expression as shown below:

$$k = 54 \times 10^6 w^2 \qquad \textbf{(Eq. 3.39)}$$

In **Equation 3.39;** k is permeability (darcy).

Second model is based on hydraulic fracturing. Fracture is assumed to have a narrow opening with a constant width all through the fracture thickness. Flowing fluid is assumed as an incompressible Newtonian fluid. Using velocity profile for the fracture and flow rate per unit length, and comparing with Darcy's equation, **Equation 3.40** is obtained. It gives the permeability and width relationship.

$$\frac{w^2}{12} = k_z \qquad \textbf{(Eq. 3.40)}$$

In **Equation 3.40;** k is permeability (in^2).

Detailed derivations of these models are presented in Chapter 4.

Chapter 4

Method of Approach

4.1 Tarmat Deformation

In order to analyze tarmat deformation, plate theory is used **[Bickford, 1998, Boresi and Schmidt, 2003, Timoshenko and Woinowski-Krieger, 1959].** In this thesis, due to the case of interest, simply supported plates having rectangular shapes and lateral dimensions that are perpendicular to x and y axes, have been focused. Two types of loading have been studied. The first one is uniform loading and the second one is non-uniform loading. Following parts of this section explain the assumptions and derivations of main equations that are used in our case, in detail.

Deformations take place in both x and y directions. Force resultants are consequences of normal and shear stresses. These force resultants are bending moments, shear forces and twisting moments which occur throughout the plane, when deformations occur. **Figure 4.1** shows a deformed plate and bending moments and shear forces on it; V represents shear force and M represents bending moment.

The way these force resultants act and their relations with each other are shown on the middle surface of the plate and on the entire plate, as shown respectively in **Figure 4.2** and **Figure 4.3. Figure 4.2** and **Figure 4.3** represent the bending and twisting moments (M's) and shear forces per unit length (Q's).

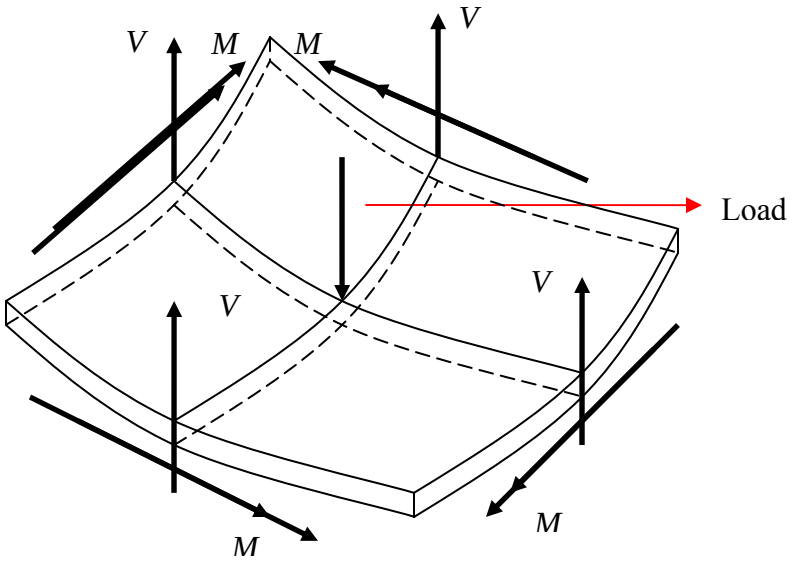

Figure 4.1: Bending moments and shear forces on a deformed plate

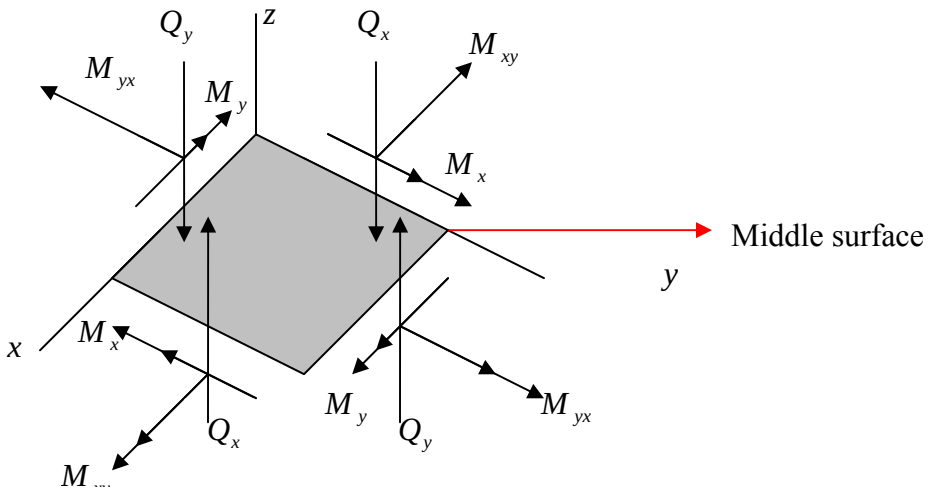

Figure 4.2: Force resultant-stress relations (middle surface of the plate)

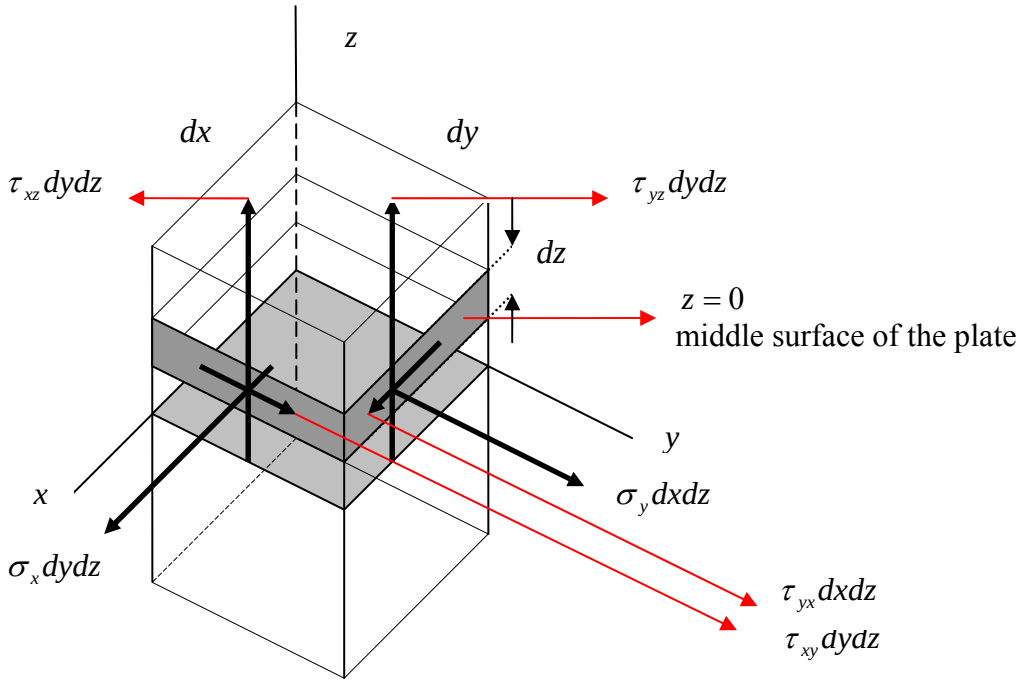

Figure 4.3: Force resultant-stress relations (entire plate)

Expressions of bending, twisting and shear moments are provided by **Equation 4.1** through **Equation 4.5.** Subscripts denote the acting directions of resultants.

$$M_x = -\int_{-h/2}^{h/2} z\sigma_x dz \qquad \textbf{(Eq. 4.1)}$$

$$M_y = -\int_{-h/2}^{h/2} z\sigma_y dz \qquad \textbf{(Eq. 4.2)}$$

$$M_{xy} = -M_{yx} = -\int_{-h/2}^{h/2} z\tau_{xy} dz \qquad \textbf{(Eq. 4.3)}$$

$$Q_x = -\int_{-h/2}^{h/2} \tau_{xz} dz \qquad \textbf{(Eq. 4.4)}$$

$$Q_y = -\int_{-h/2}^{h/2} \tau_{yz}\, dz \qquad \textbf{(Eq. 4.5)}$$

Equation of equilibrium can be developed by making use of equilibrium of forces on a free body diagram. Free body diagram and the forces acting on it are shown in **Figure 4.4.**

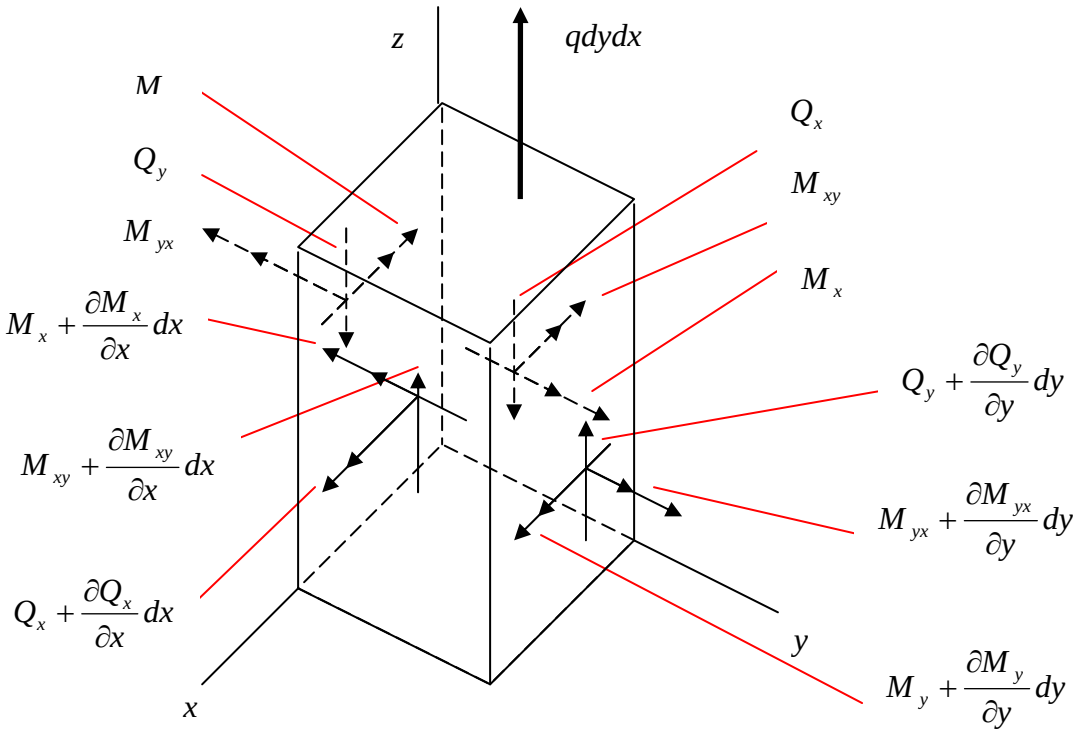

Figure 4.4: Free body diagram showing external loading and force resultants to construct equilibrium equations

Equation 4.6 and **Equation 4.7** represent the equilibrium obtained by summing the forces in z direction. **Equation 4.7** is the simplified form of **Equation 4.6:**

$$-Q_x dy - Q_y dx + \left(Q_x + \frac{\partial Q_x}{\partial x} dx\right) dy + \left(Q_y + \frac{\partial Q_y}{\partial y} dy\right) dx + q dx dy = 0 \qquad \textbf{(Eq. 4.6)}$$

$$\frac{\partial Q_x}{\partial x}+\frac{\partial Q_y}{\partial y}+q=0 \qquad \textbf{(Eq. 4.7)}$$

Equations 4.8 and **4.9** represent the equilibrium obtained by summing the moments in x direction and **Equation 4.9** is the simplified form of **Equation 4.8:**

$$\begin{aligned}&-M_{xy}dy-M_y dx+\left(M_{xy}+\frac{\partial M_{xy}}{\partial x}dx\right)dy\\&+\left(M_y+\frac{\partial M_y}{\partial y}dy\right)dx+\left(Q_y dx\right)dy=0\end{aligned} \qquad \textbf{(Eq. 4.8)}$$

$$\frac{\partial M_y}{\partial y}+\frac{\partial M_{xy}}{\partial x}+Q_y=0 \qquad \textbf{(Eq. 4.9)}$$

Equations 4.10 and **4.11** represent the equilibrium obtained by summing the moments in y direction and **Equation 4.11** is the simplified form of **Equation 4.10:**

$$\begin{aligned}&-M_{yx}dy-M_x dy+\left(M_{yx}+\frac{\partial M_{yx}}{\partial y}dy\right)dx\\&+\left(M_x+\frac{\partial M_x}{\partial x}dx\right)dy+\left(Q_x dy\right)dx=0\end{aligned} \qquad \textbf{(Eq. 4.10)}$$

$$\frac{\partial M_x}{\partial x}+\frac{\partial M_{yx}}{\partial y}+Q_x=0 \qquad \textbf{(Eq. 4.11)}$$

Taking the derivative of **Equation 4.9** with respect to y and taking the derivative of **Equation 4.11** with respect to x and substituting into **Equation 4.7** yield elimination of Q_x and Q_y. This substitution eventually leads to **Equation 4.12:**

$$\frac{\partial^2 M_x}{\partial x^2}+\frac{\partial^2 M_y}{\partial y^2}+\frac{\partial^2 M_{xy}}{\partial y\partial x}+\frac{\partial^2 M_{yx}}{\partial x\partial y}=q \qquad \textbf{(Eq. 4.12)}$$

Force resultant relations are derived by equilibrium in different directions in the free body diagram of the plate. Strain-displacement relations can be discussed since their definitions are necessary to obtain more detailed expressions.

Plate that is subjected to transverse loading with certain distribution is displaced perpendicular to its middle plane. In addition to this major displacement, there are small displacements in x and y directions. These additional displacements occur due to rotations through x and y axes.

Displacements in each direction can be expressed as in **Equation 4.13:**

$$w(x,y,z) = w_0(x,y) + zw_1(x,y), \quad u(x,y,z) = u_0(x,y) + zu_1(x,y)$$
$$v(x,y,z) = v_0(x,y) + zv_1(x,y) \qquad \textbf{(Eq. 4.13)}$$

In **Equation 4.13**; w_0 is the displacement of middle surface (z component), u_0 is the displacement of middle surface (x component), v_0 is the displacement of middle surface (y component), w_1 is displacement relative to middle surface (z component), u_1 is the displacement relative to middle surface (x component) and v_1 is the displacement relative to middle surface (y component).

In **Figure 4.5;** a view along y axis is shown, in which u is the displacement in x direction and w is the displacement in z direction. Figure would have been similar if it were drawn from a view along x axis, v being the displacement in y direction**.**

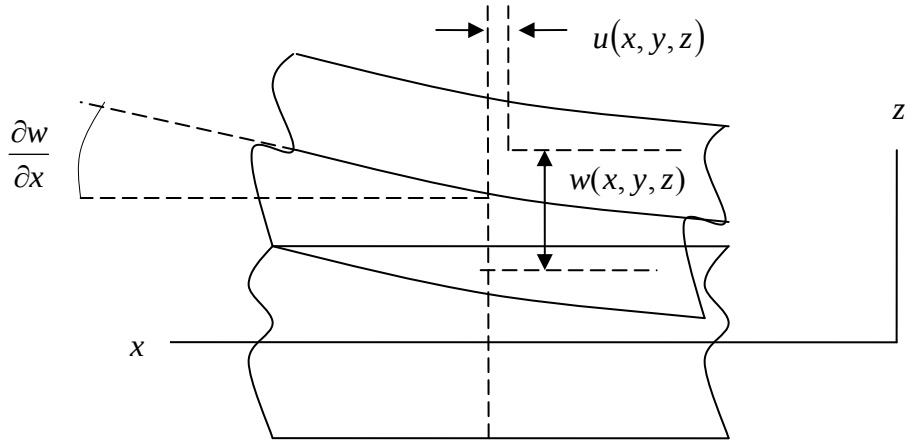

Figure 4.5: Plane deformation from a view along y axis

With the assumption of deformations being small and not being larger than half thickness of the plate of interest, strain-displacement relations are assumed linear. Linear portions of relevant equations to analyze plane deformation are given in **Equation 4.14** and **Equation 4.15.** They are written for normal strains and shear strains, respectively:

$$\varepsilon_x = \frac{\partial u}{\partial x}, \quad \varepsilon_y = \frac{\partial v}{\partial y}, \quad \varepsilon_y = \frac{\partial v}{\partial y} \qquad \textbf{(Eq. 4.14)}$$

$$\gamma_{xy} = \frac{\partial u}{\partial y} + \frac{\partial v}{\partial x}, \quad \gamma_{yz} = \frac{\partial w}{\partial y} + \frac{\partial v}{\partial z}, \quad \gamma_{xz} = \frac{\partial u}{\partial z} + \frac{\partial w}{\partial x} \qquad \textbf{(Eq. 4.15)}$$

Substitution of expressions in **Equation 4.13** into the relevant expressions in **Equation 4.14** yields expressions in **Equation 4.16:**

$$\varepsilon_x = \frac{\partial u_0}{\partial x} + \frac{\partial u_1}{\partial x}, \quad \varepsilon_y = \frac{\partial v_0}{\partial y} + \frac{\partial v_1}{\partial y}, \quad \varepsilon_z = w_1(x, y) \qquad \textbf{(Eq. 4.16)}$$

Since the thickness of the plate does not change, ε_z is equal to zero. Displacements that occur within the middle surface of the plane, u_0 and v_0 are also zero. With these assumptions the shear strains of **Equation 4.15** may be put into the form as shown by **Equation 4.17:**

$$\gamma_{xy} = z\left[\frac{\partial v_1(x,y)}{\partial x} + \frac{\partial u_1(x,y)}{\partial y}\right], \qquad \gamma_{yz} = \frac{\partial w_0(x,y)}{\partial y} + v_1(x,y)$$

$$\gamma_{xz} = \frac{\partial w_0(x,y)}{\partial x} + u_1(x,y) \qquad \textbf{(Eq. 4.17)}$$

After this reevaluation, shear deformations, γ_{yz} and γ_{xz} are assumed to be zero. These assumptions yield to **Equation 4.18:**

$$v_1 = -\frac{\partial w_0(x,y)}{\partial y}, \qquad u_1 = -\frac{\partial w_0(x,y)}{\partial x} \qquad \textbf{(Eq. 4.18)}$$

Equation 4.19, **Equation 4.20** and **Equation 4.21** summarize the displacements and strain-displacement relations:

$$u = -z\frac{\partial w}{\partial x}, \qquad v = -z\frac{\partial w}{\partial y}, \qquad w = w(x,y) \qquad \textbf{(Eq. 4.19)}$$

$$\varepsilon_x = -z\frac{\partial^2 w}{\partial x^2}, \qquad \varepsilon_y = -z\frac{\partial^2 w}{\partial y^2}, \qquad \varepsilon_z = 0 \qquad \textbf{(Eq. 4.20)}$$

$$\gamma_{xy} = -2z\frac{\partial^2 w}{\partial x \partial y}, \qquad \gamma_{yz} = 0, \qquad \gamma_{xz} = 0 \qquad \textbf{(Eq. 4.21)}$$

Having provided displacements and strain-displacement relations, now stress-strain relations may be investigated to obtain detailed expressions of bending moments, twisting moments, normal stresses and shear stresses.

Stress-strain relations which are mainly functions of Young's modulus of elasticity and Poisson's ratio are given in **Equation 4.22:**

$$\varepsilon_x = \frac{\sigma_x - \nu\sigma_y}{E}, \quad \varepsilon_y = \frac{\sigma_y - \nu\sigma_x}{E}, \quad \gamma_{xy} = \frac{\tau_{xy}}{G} = \frac{2(1+\nu)\tau_{xy}}{E} \qquad \textbf{(Eq. 4.22)}$$

Expressions in **Equation 4.22** are solved for normal and shear stresses. They are separately shown in **Equation 4.23, Equation 4.24** and **Equation 4.25,** respectively:

$$\sigma_x = \frac{E}{1-\nu^2}\left(\varepsilon_x + \nu\varepsilon_y\right) \qquad \textbf{(Eq. 4.23)}$$

$$\sigma_y = \frac{E}{1-\nu^2}\left(\varepsilon_y + \nu\varepsilon_x\right) \qquad \textbf{(Eq. 4.24)}$$

$$\tau_{xy} = \frac{E}{2(1+\nu\ )}\gamma_{xy} \qquad \textbf{(Eq. 4.25)}$$

Expressions in **Equation 4.20** and **Equation 4.21** are substituted into relevant places in **Equation 4.23, Equation 4.24** and **Equation 4.25** to obtain **Equation 4.26**, **Equation 4.27** and **Equation 4.29,** respectively:

$$\sigma_x = -\frac{Ez}{1-\nu^2}\left(\frac{\partial^2 w}{\partial x^2} + \nu\frac{\partial^2 w}{\partial y^2}\right) \qquad \textbf{(Eq. 4.26)}$$

$$\sigma_y = -\frac{Ez}{1-\nu^2}\left(\frac{\partial^2 w}{\partial y^2} + \nu\frac{\partial^2 w}{\partial x^2}\right) \qquad \textbf{(Eq. 4.27)}$$

$$\tau_{xy} = -\frac{Ez}{1-\nu^2}(1-\nu)\left(\frac{\partial^2 w}{\partial x \partial y}\right) \qquad \textbf{(Eq. 4.28)}$$

In order to obtain expressions for bending and twisting moments, **Equation 4.26**, **Equation 4.27** and **Equation 4.28** can be substituted into **Equation 4.1**, **Equation 4.2** and **Equation 4.3.** This substitution yields **Equation 4.29, Equation 4.30,** and **Equation 4.31:**

$$M_x = -\int_{-h/2}^{h/2} z\sigma_x dz = D\left(\frac{\partial^2 w}{\partial x^2} + \nu\frac{\partial^2 w}{\partial y^2}\right) \qquad \textbf{(Eq. 4.29)}$$

$$M_y = -\int_{-h/2}^{h/2} z\sigma_y dz = D\left(\frac{\partial^2 w}{\partial y^2} + \nu\frac{\partial^2 w}{\partial x^2}\right) \qquad \textbf{(Eq. 4.30)}$$

$$M_{xy} = -M_{yx} - \int_{-h/2}^{h/2} z\tau_{xy} dz = D(1-\nu)\frac{\partial^2 w}{\partial x \partial y} \qquad \textbf{(Eq. 4.31)}$$

The flexural rigidity, D, that appears in **Equation 4.29, Equation 4.30, Equation 4.31** is defined by **Equation 4.32:**

$$D = \frac{Eh^3}{12(1-\nu^2)} \qquad \textbf{(Eq. 4.32)}$$

In order to obtain expressions for normal and shear stresses, the terms; $\partial^2 w/\partial y^2 + \nu(\partial^2 w/\partial x^2)$, $\partial^2 w/\partial x^2 + \nu(\partial^2 w/\partial y^2)$ and $\partial^2 w/\partial x \partial y$, namely the displacement terms, may be eliminated. **Equation 4.33** below contains the expressions obtained by this elimination.

$$\sigma_x = -\frac{12z}{h^3}M_x, \quad \sigma_y = -\frac{12z}{h^3}M_y, \quad \tau_{xy} = -\frac{12z}{h^3}M_{xy} \qquad \textbf{(Eq. 4.33)}$$

Maximum bending stresses and maximum shear stresses occur in the middle plane. The substitution of the term $z = h/2$ into the expressions in **Equation 4.33** yields **Equation 4.34:**

$$(\sigma_x)_{\max} = \pm\frac{6M_x}{h^2}, \quad (\sigma_y)_{\max} = \pm\frac{6M_y}{h^2}, \quad (\tau_{xy})_{\max} = \pm\frac{6M_{xy}}{h^2} \qquad \textbf{(Eq. 4.34)}$$

To obtain the biharmonic equation; **Equation 4.29**, **Equation 4.30** and **Equation 4.31** are substituted into **Equation 4.12.** This substitution yields **Equation 4.35:**

$$\begin{aligned}&\frac{\partial^2}{\partial x^2}\left(D\left(\frac{\partial^2 w}{\partial x^2}+\nu\frac{\partial^2 w}{\partial y^2}\right)\right)+\frac{\partial^2}{\partial y^2}\left(D\left(\frac{\partial^2 w}{\partial y^2}+\nu\frac{\partial^2 w}{\partial x^2}\right)\right)\\&+\frac{\partial^2}{\partial y\partial x}\left(D(1-\nu)\frac{\partial^2 w}{\partial x\partial y}\right)-\frac{\partial^2}{\partial x\partial y}\left(-D(1-\nu)\frac{\partial^2 w}{\partial x\partial y}\right)=q\end{aligned} \qquad \textbf{(Eq. 4.35)}$$

Equation 4.35 can be simplified and put into the form of **Equation 4.36:**

$$D\left(\frac{\partial^4 w}{\partial x^4}+2\frac{\partial^4 w}{\partial x^2\partial y^2}+\frac{\partial^4 w}{\partial y^4}\right)=q \qquad \textbf{(Eq. 4.36)}$$

Equation **4.36** may also be written as in Equation **4.37:**

$$D\nabla^2\left(\nabla^2 w\right)=q \qquad \textbf{(Eq. 4.37)}$$

In our study, all of the edges of the plate are considered to have simply supported boundary conditions. Shape of the plate is square, which is a rectangle having equal lateral dimensions. There are two main conditions to be satisfied for simply supported edges. First one is, displacement w must be equal to zero and the second one is moment which has a coinciding direction with the direction of the edge must be equal to zero.

On the edges at which y is constant, **Equation 4.38** should be satisfied as boundary conditions:

$$w = 0\,, \quad M_y = D\left(\frac{\partial^2 w}{\partial y^2} + \nu \frac{\partial^2 w}{\partial x^2}\right) = 0 \qquad \textbf{(Eq. 4.38)}$$

On this edges, w being equal to zero leads to $\partial^2 w/\partial x^2 \equiv 0$. However, in general $\partial w/\partial y$ and Q_y are not equal to zero. This leads another way of expressing boundary conditions with **Equation 4.39:**

$$w = 0\,, \; \frac{\partial^2 w}{\partial y^2} = 0 \qquad \textbf{(Eq. 4.39)}$$

On the edges at which x is constant, **Equation 4.40** should be satisfied as boundary conditions:

$$w = 0\,, \quad M_x = D\left(\frac{\partial^2 w}{\partial x^2} + \nu \frac{\partial^2 w}{\partial y^2}\right) = 0 \qquad \textbf{(Eq. 4.40)}$$

Similarly, on this edges, w being equal to zero leads to $\partial^2 w/\partial y^2 \equiv 0$. However, in general $\partial w/\partial x$ and Q_x are not equal to zero. This leads another way of expressing boundary conditions with **Equation 4.41:**

$$w = 0\,, \quad \frac{\partial^2 w}{\partial x^2} = 0 \qquad \textbf{(Eq. 4.41)}$$

Until this point, general information about stress, strain and displacement relations have been provided. Derivation of general expressions of bending and twisting moments, stresses have been considered. Then the shape and boundary condition assumptions have been presented. At this point, appropriate solution for rectangular plate problems with simply supported opposite edges can be considered. It should be noted that transverse loading may be non-uniform as well as uniform. Each type of loading is basically shown in **Figure 4.6** followed by separate considerations of each type.

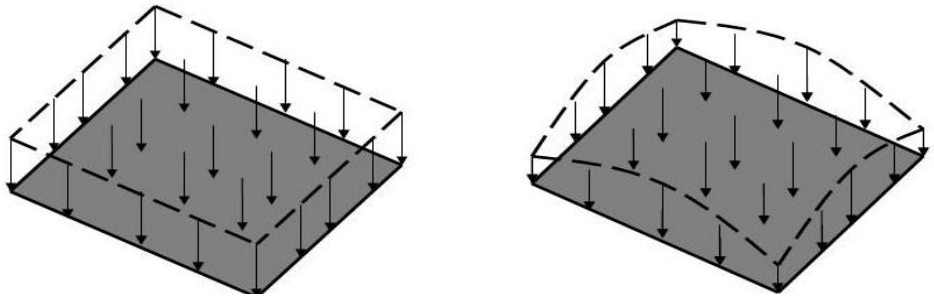

Figure 4.6: Uniformly (a) and non-uniformly (b) loaded rectangular plates

General solution for transverse displacement $w(x,y)$ is expressed by **Equation 4.42** below. This equation satisfies the requirements of simply supported boundary conditions:

$$w(x,y) = w_{mn} \sin\frac{m\pi x}{a} \sin\frac{n\pi y}{b} \qquad \textbf{(Eq. 4.42)}$$

Equation 4.42 may also be put in a form that is expressed by **Equation 4.43** in which superposition is used:

$$w(x,y) = \sum_{m=1}\sum_{n=1} w_{mn} \sin\frac{m\pi x}{a} \sin\frac{n\pi y}{b} \qquad \textbf{(Eq. 4.43)}$$

Solution for transverse loading is expressed by **Equation 4.44:**

$$q(x,y) = \sum_{m=1}\sum_{n=1} q_{mn} \sin\frac{m\pi x}{a} \sin\frac{n\pi y}{b} \qquad \textbf{(Eq. 4.44)}$$

Substituting **Equation 4.43** and **Equation 4.44** into **Equation 4.37** yields **Equation 4.45:**

$$D\sum_{m=1}\sum_{n=1} w_{mn}\left(\left(\frac{m\pi}{a}\right)^2+\left(\frac{n\pi}{b}\right)^2\right)^2 \sin\frac{m\pi x}{a}\sin\frac{n\pi y}{b} = \sum_{m=1}\sum_{n=1} q_{mn}\sin\frac{m\pi x}{a}\sin\frac{n\pi y}{b} \quad \textbf{(Eq. 4.45)}$$

Solving **Equation 4.45** for w_{mn} yields to Equation **4.46:**

$$w_{mn} = \frac{q_{mn}}{D\left(\left(\frac{m\pi}{a}\right)^2+\left(\frac{n\pi}{b}\right)^2\right)^2} \quad \textbf{(Eq. 4.46)}$$

In case of a uniform loading, where $q = q_0$, q_{mn} may be obtained by **Equation 4.47** which holds when m and n are odd:

$$q_{mn} = \frac{16q_0}{mn\pi^2} \quad \textbf{(Eq. 4.47)}$$

Substitution of **Equation 4.47** into **Equation 4.46**, and then the obtained expression into **Equation 4.43** yields **Equation 4.48:**

$$w = \frac{16q_0}{\pi^6 D}\sum_{m,odd}\sum_{n,odd}\frac{\sin\frac{m\pi x}{a}\sin\frac{n\pi y}{b}}{mn\left(\left(\frac{m}{a}\right)^2+\left(\frac{n}{b}\right)^2\right)^2} \quad \textbf{(Eq. 4.48)}$$

In addition to transverse displacement derivations, bending moments and twisting moments can be derived as in the following equations that are **Equation 4.49, Equation 4.50** and **Equation 4.51,** respectively:

$$M_x = D(\frac{\partial^2 w}{\partial x^2} + \nu \frac{\partial^2 w}{\partial y^2})$$

$$= -\frac{16q_0}{\pi^4} \sum_{m,odd} \sum_{n,odd} \frac{\left(\frac{m^2}{a^2} + \nu \frac{n^2}{b^2}\right) \sin\frac{m\pi x}{a} \sin\frac{n\pi y}{b}}{mn\left(\left(\frac{m}{a}\right)^2 + \left(\frac{n}{b}\right)^2\right)^2} \qquad \textbf{(Eq. 4.49)}$$

$$M_y = D(\frac{\partial^2 w}{\partial y^2} + \nu \frac{\partial^2 w}{\partial x^2})$$

$$= -\frac{16q_0}{\pi^4} \sum_{m,odd} \sum_{n,odd} \frac{\left(\frac{n^2}{b^2} + \nu \frac{m^2}{a^2}\right) \sin\frac{m\pi x}{a} \sin\frac{n\pi y}{b}}{mn\left(\left(\frac{m}{a}\right)^2 + \left(\frac{n}{b}\right)^2\right)^2} \qquad \textbf{(Eq. 4.50)}$$

$$M_{xy} = -M_{yx} = D(1-\nu)(\frac{\partial^2 w}{\partial y \partial x})$$

$$= \frac{16(1-\nu)q_0}{\pi^4 ab} \sum_{m,odd} \sum_{n,odd} \frac{\cos\frac{m\pi x}{a} \cos\frac{n\pi y}{b}}{\left(\left(\frac{m}{a}\right)^2 + \left(\frac{n}{b}\right)^2\right)^2} \qquad \textbf{(Eq. 4.51)}$$

These expressions being appropriate for rectangular plates under uniform loading that are simply supported from all edges, can be evaluated until each series converges.

In the case in which boundary conditions and the plate shape is similar, while the plate is under non-uniform loading that is distributed all over the surface, q_{mn} is expressed as in **Equation 4.52:**

$$q = q_0 \sin\frac{m\pi x}{a} \sin\frac{n\pi y}{b} \qquad \textbf{(Eq. 4.52)}$$

In this equation q_0 refers to the intensity of the loading at the center of the plate. **Equation 4.52** can be substituted into **Equation 4.36** which yields **Equation 4.53:**

$$D\left(\frac{\partial^4 w}{\partial x^4}+2\frac{\partial^4 w}{\partial x^2\partial y^2}+\frac{\partial^4 w}{\partial y^4}\right)=q_0\sin\frac{m\pi x}{a}\sin\frac{n\pi y}{b} \qquad \textbf{(Eq. 4.53)}$$

For simplicity, m and n are assumed to be equal to zero. Then, **Equation 4.42** is substituted into **Equation 4.53.** This substitution provides the expression for w_{mn} as it is solved for it. This solution is given by **Equation 4.54:**

$$w_{mn}=\frac{q_0}{D\pi^4\left(\frac{1}{a^2}+\frac{1}{b^2}\right)^2} \qquad \textbf{(Eq. 4.54)}$$

Equation 4.54 is placed in **Equation 4.42** to obtain the deflection surface that is caused by non-uniform transverse loading. **Equation 4.55** is the expression for representing the deflection at a given x and y coordinates:

$$w=\frac{q_0}{D\pi^4\left(\frac{1}{a^2}+\frac{1}{b^2}\right)^2}\sin\frac{\pi x}{a}\sin\frac{\pi y}{b} \qquad \textbf{(Eq. 4.55)}$$

In addition to transverse displacement derivations, bending moments and twisting moments can be derived as in the following equations that are **Equation 4.56**, **Equation 4.57** and **Equation 4.58,** respectively:

$$M_x=D(\frac{\partial^2 w}{\partial x^2}+\nu\frac{\partial^2 w}{\partial y^2})=\frac{q_0}{\pi^2}\frac{\left(\frac{1}{a^2}+\nu\frac{1}{b^2}\right)\sin\frac{\pi x}{a}\sin\frac{\pi y}{b}}{\left(\left(\frac{1}{a}\right)^2+\left(\frac{1}{b}\right)^2\right)^2} \qquad \textbf{(Eq. 4.56)}$$

$$M_y = D\left(\frac{\partial^2 w}{\partial y^2} + \nu \frac{\partial^2 w}{\partial x^2}\right) = \frac{q_0}{\pi^2} \frac{\left(\frac{1}{b^2} + \nu \frac{1}{a^2}\right) \sin\frac{\pi x}{a} \sin\frac{\pi y}{b}}{\left(\left(\frac{1}{a}\right)^2 + \left(\frac{1}{b}\right)^2\right)^2} \qquad \textbf{(Eq. 4.57)}$$

$$M_{xy} = -M_{yx} = D(1-\nu)\left(\frac{\partial^2 w}{\partial y \partial x}\right) = \frac{(1-\nu) q_0}{\pi^2 ab} \frac{\cos\frac{\pi x}{a} \cos\frac{\pi y}{b}}{\left(\left(\frac{1}{a}\right)^2 + \left(\frac{1}{b}\right)^2\right)^2} \qquad \textbf{(Eq. 4.58)}$$

Since these expressions are simplified before derivation by taking *m* and *n* as 1, evaluation of series has not been necessary in the case of non-uniform loading.

A detailed discussion regarding the comparison of uniform and non-uniform loading is presented in Chapter 5.

4.2 Failure Analysis

In order to evaluate the tarmat behavior to the instant of geomechanical failure, tarmat deformation analysis should be forwarded to a failure criterion.

In maximum shear stress failure criterion, three different cases can occur which depend on the principle stresses. They are explained in Chapter 3 with details. Principle stresses are obtained by **Equation 4.59** below:

$$\sigma_{1,2} = \pm \frac{\sigma_x + \sigma_y}{2} \pm \sqrt{\frac{\sigma_x - \sigma_y}{2} + \tau_{xy}^2} \qquad \textbf{(Eq. 4.59)}$$

In **Equation 4.59;** $\sigma_{1,2}$ is first and second principle stresses (psi), which can be followed by subscript respectively.

First case which may occur is $\sigma_1 \rangle \sigma_2 \rangle 0$, $\sigma_3 = 0$, second case which may occur is $\sigma_2 \langle \sigma_1 \langle 0$, $\sigma_3 = 0$ and third case which may occur is $\sigma_1 \rangle 0$, $\sigma_2 \langle 0$, $\sigma_3 = 0$.

In this stage of our problem, first and second cases may be used both. In tarmat deformation analysis, after bending and twisting moment calculations, if expressions in **Equation 4.34** are used by choosing negative sign convention, first case becomes the case to select. However, if they are used by choosing positive sign convention, second case is appropriate to select.

In the first case maximum shear stress is calculated by **Equation 4.60** where in second case it is calculated by **Equation 4.61**. They are provided below:

$$\tau_{\max} = \frac{\sigma_1}{2} \qquad \textbf{(Eq. 4.60)}$$

$$\tau_{\max} = \frac{|\sigma_2|}{2} \qquad \textbf{(Eq. 4.61)}$$

They are concluded to lead to same failure points. Second case is chosen to use in our analysis. Following interpretations help to explain the analysis in detail.

Due to Mohr's circle, maximum shear stress is given by **Equation 4.62** which is;

$$\tau_{\max} = \frac{\sigma_{YS}}{2} \qquad \textbf{(Eq. 4.62)}$$

In **Equation 4.62;** $\tau_{\max}$ is maximum shear stress (psi) and σ_{YS} is yield strength (psi).

By combining **Equation 4.61** and **Equation 4.62;** criteria that needs to be satisfied in order for the material not to fail is obtained. This is shown by **Equation 4.63** and **Equation 4.64:**

$$\frac{|\sigma_2|}{2} = \frac{\sigma_{YS}}{2} \qquad \textbf{(Eq. 4.63)}$$

$$|\sigma_2| = \sigma_{YS} \qquad \textbf{(Eq. 4.64)}$$

This means that if $|\sigma_2|$ exceeds σ_{YS} of the material, failure occurs **[Gere-2001, Bickford-1998].**

4.3 Pressure Transient Model

This stage of the analysis is dealing with reservoir depletion that occurs at the upper part of the composite system of interest. Conventional well test models have been used to calculate the change of pressure in the single phase, square shaped reservoir. Well is assumed to be located at the middle of the reservoir. **Figure 4.7** shows the orientation of well point and observation points in the selected conventional well test case.

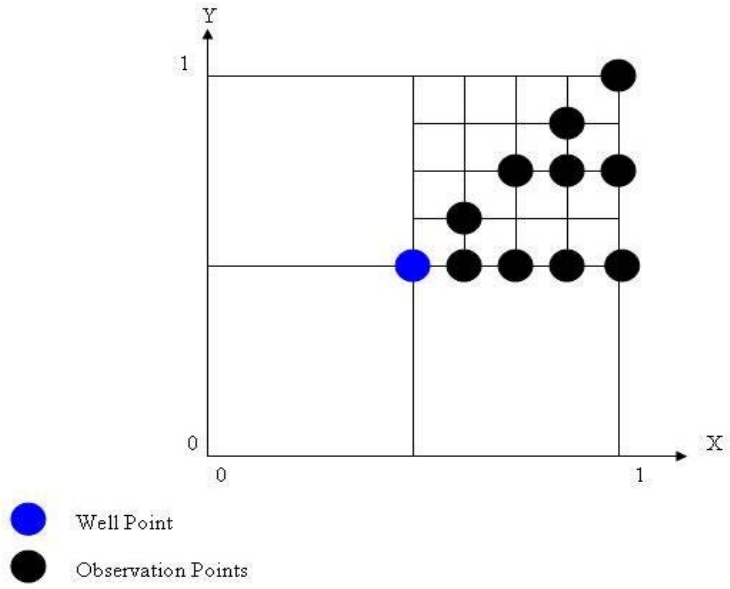

Figure 4.7: Reservoir configuration with locations of well point and observation points

Table 4-1 shows the dimensionless pressure drops that would be encountered at a specific dimensionless time, due to well point and observation points shown in **Figure 4.7.**

Table 4-1: Dimensionless Pressure Drop and Corresponding Dimensionless Time at Well Point and Observation Points, $\sqrt{A}/r_w$ =2,000 **[Earlougher, *et al.*, 1968]**

	Dimensionless Pressure Drop At Well Point and Observation Points										
	X=0.5000	X=0.6250	X=0.6250	X=0,7500	X=0.7500	X=0.8750	X=0.8750	X=0.8750	X=1.0000	X=1.0000	X=1.0000
t_{DA}	Y=0.5000	Y=0.5000	Y=0.6250	Y=0.5000	Y=0.7500	Y=0.5000	Y=0.7500	Y=0.8750	Y=0.5000	Y=0.7500	Y=1.0000
0.002	4.898	0.026	0.002	0.000	0.000	0.000	0.000	0.000	0.000	0.000	0.000
0.003	5.101	0.068	0.011	0.000	0.000	0.000	0.000	0.000	0.000	0.000	0.000
0.004	5.245	0.114	0.026	0.002	0.000	0.000	0.000	0.000	0.000	0.000	0.000
0.005	5.356	0.161	0.046	0.006	0.000	0.000	0.000	0.000	0.000	0.000	0.000
0.006	5.447	0.205	0.068	0.011	0.000	0.000	0.000	0.000	0.000	0.000	0.000
0.007	5.525	0.248	0.091	0.018	0.001	0.001	0.000	0.000	0.000	0.000	0.000
0.008	5.591	0.287	0.114	0.026	0.002	0.001	0.000	0.000	0.000	0.000	0.000
0.009	5.650	0.324	0.138	0.035	0.004	0.002	0.000	0.000	0.000	0.000	0.000
0.010	5.703	0.359	0.161	0.046	0.006	0.003	0.001	0.000	0.000	0.000	0.000
0.020	6.049	0.621	0.359	0.161	0.046	0.035	0.012	0.004	0.011	0.004	0.001
0.030	6.252	0.794	0.507	0.268	0.103	0.088	0.040	0.018	0.044	0.022	0.006
0.040	6.397	0.923	0.622	0.363	0.165	0.149	0.080	0.044	0.091	0.053	0.022
0.050	6.510	1.028	0.719	0.447	0.228	0.213	0.128	0.080	0.147	0.095	0.050
0.060	6.605	1.118	0.804	0.524	0.290	0.277	0.181	0.124	0.207	0.143	0.087
0.070	6.689	1.198	0.882	0.597	0.353	0.342	0.237	0.174	0.268	0.196	0.132
0.080	6.765	1.273	0.954	0.666	0.416	0.406	0.295	0.228	0.330	0.253	0.183
0.090	6.837	1.343	1.023	0.733	0.479	0.470	0.355	0.285	0.393	0.311	0.237
0.100	6.906	1.411	1.090	0.799	0.542	0.534	0.415	0.343	0.455	0.371	0.294
0.200	7.547	2.050	1.727	1.434	1.170	1.164	1.039	0.963	1.083	0.993	0.910
0.300	8.175	2.679	2.356	2.062	1.798	1.792	1.668	1.591	1.712	1.621	1.538
0.400	8.804	3.307	2.984	2.690	2.427	2.420	2.296	2.220	2.340	2.250	2.167
0.500	9.432	3.935	3.612	3.319	3.055	3.049	2.924	2.848	2.968	2.878	2.795
0.600	10.060	4.564	4.241	3.947	3.683	3.677	3.553	3.476	3.597	3.506	3.423
0.700	10.689	5.192	4.869	4.575	4.312	4.305	4.181	4.105	4.225	4.135	4.052
0.800	11.317	5.820	5.497	5.204	4.940	4.934	4.809	4.733	4.853	4.763	4.680
0.900	11.945	6.449	6.126	5.832	5.568	5.562	5.438	5.361	5.482	5.391	5.308
1.000	12.574	7.077	6.754	6.460	6.197	6.190	6.066	5.990	6.110	6.019	5.937
2.000	18.857	13.360	13.037	12.743	12.480	12.473	12.349	12.273	12.393	12.303	12.220
3.000	25.140	19.643	19.320	19.027	18.763	18.757	18.632	18.556	18.676	18.586	18.503
4.000	31.423	25.926	25.603	25.310	25.046	25.040	24.915	24.839	24.959	24.869	24.786
5.000	37.706	32.210	31.887	31.593	31.329	31.323	31.199	31.122	31.243	31.152	31.069
6.000	43.989	38.493	38.170	37.876	37.612	37.606	37.482	37.405	37.526	37.435	37.352
7.000	50.273	44.776	44.453	44.159	43.896	43.889	43.765	43.689	43.809	43.719	43.636
8.000	56.556	51.059	50.736	50.443	50.179	50.172	50.048	49.972	50.092	50.002	49.919
9.000	62.839	57.342	57.019	56.726	56.462	56.456	56.331	56.255	56.375	56.285	56.202
10.000	69.122	63.625	63.302	63.009	62.745	62.739	62.614	62.538	62.658	62.568	62.485
12.000	81.688	76.192	75.869	75.575	75.311	75.305	75.181	75.104	75.225	75.134	75.052
15.000	100.538	95.041	94.718	94.425	94.161	94.155	94.030	93.954	94.074	93.984	93.901
20.000	131.954	126.457	126.134	125.840	125.577	125.570	125.446	125.370	125.490	125.400	125.317
30.000	194.785	189.289	188.966	188.672	188.408	188.402	188.278	188.201	188.322	188.231	188.148

Dimensionless pressure drop values in **Table 4-1** are tabulated with the assumption that $\sqrt{A}/r_w$ is equal to 2,000**.** However, if this is not the case, values displayed in table should

be fixed for the value obtained for $\sqrt{A}/r_w$ for the case of interest **[Earlougher, 1977].** This correction should be done at the well point only and can be conducted as shown by **Equation 4.65**:

$$P' - \ln(2{,}000) + \ln\left(\frac{\sqrt{A}}{r_w}\right) = P'' \qquad \textbf{(Eq. 4.65)}$$

In **Equation 4.65;** A is area of interest (ft^2), r_w is well bore radius (ft), P' is the dimensionless pressure drop at the well point as given for $\sqrt{A}/r_w$ =2,000 and P'' is the corrected dimensionless pressure drop for the relevant $\sqrt{A}/r_w$ **.**

In order to find the relationship between actual pressure and actual time, the standard computational procedure of classical well test model is followed **[Earlougher, 1977, Lee, 1982].** In this procedure, dimensionless time should be converted to actual time and dimensionless pressure should be converted into actual pressure. Dimensionless production rate is used as an intermediate step in these calculations. **Equation 4.66** is an expression used for dimensionless flow rate, which is suitable for our case:

$$q_D = \frac{\gamma B q_p \mu}{khP_i} \qquad \textbf{(Eq. 4.66)}$$

In **Equation 4.66;** q_D is dimensionless flow rate, γ is the appropriate constant for the units used, B is formation volume factor (STB/RB), q_p is production rate (STB/d), μ is viscosity (cp), k is permeability (md), h is thickness (ft) and P_i is initial pressure of the reservoir (psi).

Equation 4.67; is an expression used for dimensionless pressure, which is suitable for our case:

$$\Delta P_D = \frac{P_i - P}{P_i q_D} \qquad \textbf{(Eq. 4.67)}$$

In **Equation 4.67;** ΔP_D is dimensionless pressure drop and P is actual pressure at a given time (psi).

Equation 4.67 is solved for pressure as expressed by **Equation 4.68:**

$$P = P_i - \Delta P_D P_i q_D \qquad \textbf{(Eq. 4.68)}$$

Equation 4.69 is an expression used for dimensionless time:

$$t_D = \frac{\lambda k t}{\phi \mu c r_w^2} \qquad \textbf{(Eq. 4.69)}$$

In **Equation 4.69**; t_D is dimensionless time, λ is the appropriate constant for the units used, t is the real time (hours), c is the compressibility, (psi^{-1}) and ϕ is porosity.

However, it is necessary to evaluate the dimensionless time for the area of our interest, which contains a well in the middle of it. These expressions are provided in **Equation 4.70** and **Equation 4.71,** respectively:

$$t_{DA} = t_D \frac{r_w^2}{A} \qquad \textbf{(Eq. 4.70)}$$

$$t_{DA} = \frac{\lambda k t}{\phi \mu c A} \qquad \textbf{(Eq. 4.71)}$$

Equation 4.71 is solved for actual time to which is expressed by **Equation 4.72:**

$$t = \frac{t_{DA} \phi \mu c A}{\lambda k} \qquad \textbf{(Eq. 4.72)}$$

Assumed reservoir properties are influential in this procedure. Oil production rates range from 1,000 STB/d to 10,000 STB/d and is one of the parameters with the most significant influence in the relationship between pressure and time. As production rate increases, a certain pressure differential is reached in a shorter period of time. This means that, as unloading occurs with a higher rate, critical pressures are reached faster. The dimensions of the discharge area are also very important and 51.75 acres and 200 acres are used in this analysis. Effects of influential parameters are discussed in Chapter 5 in detail. **Table 4.3** has the information of assigned properties of the reservoir.

Table 4-2: Assigned Properties of Reservoir

Property	Value	Unit
μ	0.72	cp
Ø	0.25	fraction
B	1.3	rb/stb
k	400	md
h	200	ft
c	0.0000015	psi^{-1}
r_w	0.5	ft
P_i	9,000	psi

With assigned properties of the reservoir and a certain production rate, pressure differential versus time graphs are obtained. This study can be done for a number of locations within the reservoir, since pressure distribution throughout the reservoir can be determined. However, main interest is the center, due to the fact that critical pressure that determines the instant of failure occurs at the center.

4.4 Fracture Width Analysis

This part presents the approach that is taken in fracture width analysis. In fracture width analysis, two different hydraulic fracturing models have been used as have been introduced in Chapter 3. First one is the PKN model and second one is the KGD model. They both relate hydraulic fracture width to properties of fluid and rock to be fractured; in a specific case of hydraulic fracturing. Fluid in our model is water that would communicate with the upper layers of the composite system and rock in our model is tarmat that would fail by the disturbance of pressure differential.

In both models; influential fluid properties are viscosity and specific gravity and influential rock properties are Poisson's ratio, Young's modulus of elasticty. Other properties depending on the case are; fluid injection rate and fracture length. One more property that is not influential in PKN model but is influential in KGD model is fracture thickness.

Inputs into the analysis protocol followed in this study are viscosity and specific gravity of water, Poisson's ratio and Young's Modulus of Elasticiy of tarmat, reservoir production rate and thickness of tarmat. Reservoir production rate is substituted for the fluid injection rate. The reason for this substitution is that the effect of fluid injection rate in a hydraulic fracturing case is similar to the effect of reservoir production rate in our geomechanical failure case; as both of them are expected to create a similar pressure differential in magnitude and direction. The problem has been approached inversely, to estimate fracture width as a function of reservoir production rate. Another input, thickness of tarmat, is substituted for fracture length. This is due to the reason that; in a

hydraulic fracturing case, fracture length is the parameter that helps to express the penetration of the created crack while in the case of our interest, penetration of the crack is expressed by tarmat thickness. On the other hand, fracture thickness that comes into the picture in only KGD model; corresponds to fracture length in the analyzed case. PKN model and KGD model are in agreement when the fracture thickness is assumed to be as long as the line that is drawn at the points on the plate where shear stress is 99 per cent of the maximum shear stress.

Figure 4.8 and **Figure 4.9** explains fracture thickness and fracture length orientation for a hydraulic fracturing case and for our case, respectively.

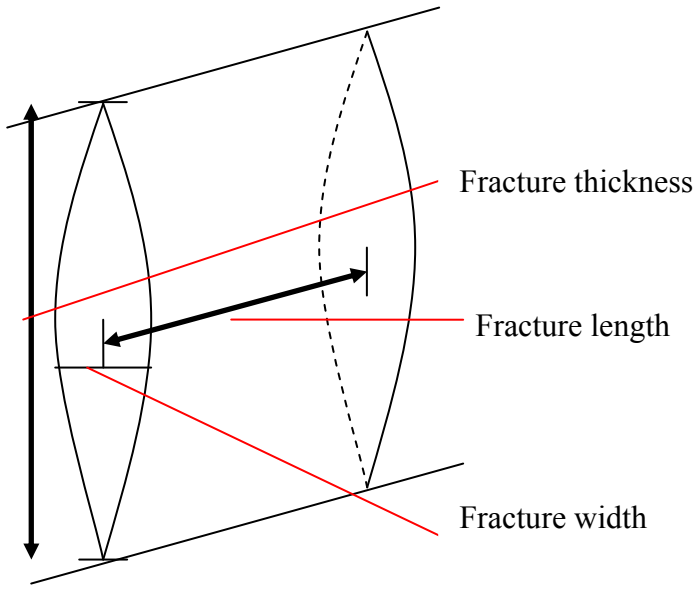

Figure 4.8: Fracture length, fracture width and fracture thickness in a hydraulic crack

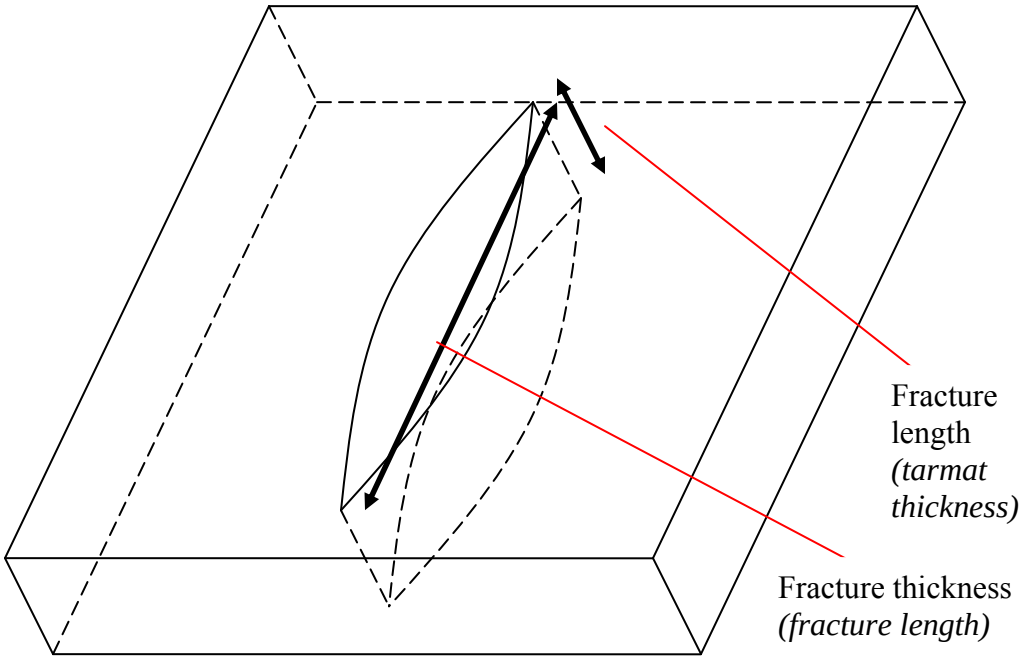

Figure 4.9: Fracture length and fracture thickness in the case of interest

The fracture width is expressed by **Equation 4.73** and **Equation 4.74,** for the PKN and KGD models, respectively and G, which is an input parameter in each model is expressed by **Equation 4.75**:

$$w = 0.3\left[\frac{q\mu(1-\nu)(h_0/2)}{G}\right]^{1/4}\left(\frac{\pi}{4}\gamma\right) \qquad \textbf{(Eq. 4.73)}$$

$$w = 0.29\left[\frac{q\mu(1-\nu)(h_0/2)^2}{Gh_f}\right]^{1/4}\left(\frac{\pi}{4}\right) \qquad \textbf{(Eq. 4.74)}$$

$$G = \frac{E}{2(1+\nu)} \qquad \textbf{(Eq. 4.75)}$$

In **Equation 4.73**, **Equation 4.74** and **Equation 4.75;** μ is viscosity of fluid *(water,* cp*),* γ is specific gravity of fluid *(water),* v is Poisson's ratio of rock *(tarmat),* E is Young's modulus of elasticity of rock *(tarmat,* psi*),* G is shear modulus of rock *(tarmat*, psi*),* q is flow rate *(production rate,* BPM*),* $(h_0/2)$ is half fracture length *(half tarmat thickness,* ft*),* and h_f is fracture thickness *(fracture length,* ft*)* **[Economides, 1992].**

4.5 Permeability Analysis

This stage of the analysis focuses on the fracture permeability that would be established after the geomechanical failure of tarmat followed by creation of a fracture with a certain width. Two different approaches have been used to estimate fracture permeability. First one is referred as viscous flow of wetting fluids through smooth fractures of constrant width **[Craft and Hawkins, 1959].** Second one is referred as flow of hydraulic fracturing fluids through the induced fractures **[Yew, 1997].** How they are used in this stage of our analysis is explained in detail in the following sections.

4.5.1 Flow through Fractures

The first approach that focuses on viscous flow of wetting fluids through smooth fractures of constrant width, is based on a particular case of fluid flow in reservoirs. For capillary flow in porous media, Poiseuille's law for capillary flow relates flow rate to fluid viscosity, pressure differential, radius and length of the capillary tube through which flow occurs. Then, permeability can be related to the radius. In this stage of the analysis,

fracture permeability is related to fracture width, by following the same derivation procedure that leads to Poiseuille's Law for Capillary Flow in a capillary flow case. Only difference is that flow that takes place in the case of our interest is through a fracture of constant width.

Derivation can be started by writing an expression for viscous forces that would be created within the flowing fluid:

$$F_v = \mu A \frac{dv}{dx} \qquad \textbf{(Eq. 4.76)}$$

In **Equation 4.76**; F_v is viscous force, (dynes), μ is fluid viscosity, (poises), A is area that the flowing fluid wets while flowing, (cm^2) and $\frac{dv}{dx}$ is the velocity gradient, [cm/sec)/cm].

Area that is wetted by the flowing fluid is twice the lateral areas of each fracture wing. This is expressed by **Equation 4.77**:

$$A = 2h_0 h_f \qquad \text{(Eq. } \textbf{4.77}\text{)}$$

In **Equation 4.77**; h_f is thickness of the fracture (cm) and h_0 is thickness of the tarmat (cm).

Equation 4.77 is substituted into **Equation 4.76** to obtain **Equation 4.78:**

$$F_v = \mu\left(2h_0 h_f\right)\frac{dv}{dx} \qquad \textbf{(Eq. 4.78)}$$

In addition to viscous forces, the pressure differential through the penetration length of the fracture creates another force through the fracture. This force may be referred as the

driving force. Since the flowing fluid is not accelerating, driving forces and viscous forces add up to zero. **Equation 4.79** shows the relevant force balance:

$$\mu\left(2h_0h_f\right)\frac{dv}{dx}+A'\left(P_1-P_2\right)=0 \qquad \textbf{(Eq. 4.79)}$$

In **Equation 4.79;** $\left(P_1-P_2\right)$ is pressure differential acting on the cross sectional area of fluid flow (dyne/cm^2) and A' is cross sectional area that pressure differential acts on (cm^2).

Separating velocity gradient terms and integrating, **Equation 4.80** and **Equation 4.81** are obtained respectively:

$$dv=-\frac{A'\left(P_1-P_2\right)dx}{\mu\left(2h_0h_f\right)} \qquad \textbf{(Eq. 4.80)}$$

$$v=-\frac{A'\left(P_1-P_2\right)x}{\mu\left(2h_0h_f\right)}+C \qquad \textbf{(Eq. 4.81)}$$

In **Equation 4.80** and **Equation 4.81;** C is the integration constant and x represents the lateral extent of width. Since v would be equal to zero where x is equal to w, **Equation 4.81** is solved for this situation to find an expression for C, shown by **Equation 4.82:**

$$C=\frac{A'\left(P_1-P_2\right)w}{\mu\left(2h_0h_f\right)} \qquad \textbf{(Eq. 4.82)}$$

In **Equation 4.82;** w is width of the fracture (cm).

Equation 4.82 is substituted back to the **Equation 4.81** to obtain **Equation 4.83:**

$$v=\frac{A'\left(P_1-P_2\right)}{\mu\left(2h_0h_f\right)}\left(-x+w\right) \qquad \textbf{(Eq. 4.83)}$$

At this point, fluid flow rate, should be related to the derived velocity expression. **Equation 4.84** is general expression for a relevant element:

$$q = \int_0^q dq \qquad \textbf{(Eq. 4.84)}$$

In **Equation 4.84**; q is fluid flow rate (cm^3/sec).

Flow rate is expressed in terms of cross sectional area and velocity as in **Equation 4.85** and put into the differential form as in **Equation 4.86:**

$$q = vA' \qquad \textbf{(Eq. 4.85)}$$

$$dq = vdA' \qquad \textbf{(Eq. 4.86)}$$

Equation 4.86 is substituted to **Equation 4.84** to obtain **Equation 4.87:**

$$q = \int_0^q vdA' \qquad \textbf{(Eq. 4.87)}$$

Cross sectional area of flow through fracture is expressed in terms of fracture thickness and width. This expression and its differential form are given in **Equation 4.88** and **Equation 4.89:**

$$A' = h_f x \qquad \textbf{(Eq. 4.88)}$$

$$dA' = h_f dx \qquad \textbf{(Eq. 4.89)}$$

Equation 4.83 and **Equation 4.89** are substituted to **Equation 4.87** to obtain **Equation 4.90:**

$$q = \int_0^w \frac{x h_f (P_1 - P_2)}{\mu(2h_0 h_f)}(-x + w)h_f \, dx \qquad \textbf{(Eq. 4.90)}$$

Separating parameters that are independent from x and integrating **Equation 4.90** through the entire width of the fracture, **Equation 4.91**, **Equation 4.92** and **Equation 4.93** are obtained:

$$q = \frac{(P_1 - P_2)h_f}{\mu(2h_0)} \int_0^w x(-x + w)dx \qquad \textbf{(Eq. 4.91)}$$

$$q = \frac{(P_1 - P_2)h_f}{\mu(2h_0)} \left[\frac{-2x^3 + 3wx^2}{6} \right]_0^W \qquad \textbf{(Eq. 4.92)}$$

$$q = \frac{(P_1 - P_2)h_f w^3}{12\mu h_0} \qquad \textbf{(Eq. 4.93)}$$

Equation 4.93 can also be written as in **Equation 4.94**, since multiplication of fracture thickness and fracture width gives cross sectional area. This can be referred as the flow equation obtained for wetting fluids through smooth fractures of constant width:

$$q = \frac{(P_1 - P_2)A' w^2}{12\mu h_0} \qquad \textbf{(Eq. 4.94)}$$

Equation 4.95; as shown below is the form of Darcy's law, which is expressed in similar units with **Equation 4.94:**

$$q = \frac{9.86 \times 10^{-9} kA(P_1 - P_2)}{\mu L} \qquad \textbf{(Eq. 4.95)}$$

In **Equation 4.95;** k is the formation permeability (darcy).

Equation 4.94 and **Equation 4.95** are combined and solved for k as being permeability of the fracture. **Equation 4.96** is obtained as an expression which provides fracture permeability as a function of fracture width:

$$k = 54 \times 10^6 w^2 \qquad \textbf{(Eq. 4.96)}$$

In **Equation 4.96,** w is in inches and k is in darcies.

4.5.2 Hydraulic Fracturing

In this model, fracture is assumed to have a narrow opening with a constant width all through the fracture thickness. Flowing fluid is assumed to be an incompressible Newtonian fluid, which is valid for our case. Ignoring the negligible pressure differential created through the width of the fracture, velocity profile can be expressed as in **Equation 4.97**. Subscript denotes the flow direction:

$$v_z = -\frac{1}{2\mu}\left[\left(\frac{w}{2}\right)^2 - x^2\right]\frac{\partial P}{\partial z} \qquad \textbf{(Eq. 4.97)}$$

In **Equation 4.97;** v_z is velocity, μ is fluid viscosity, w is fracture width**,** $\frac{\partial P}{dz}$ is pressure gradient **[Howard and Fast, 1970].**

Volumetric flow rate per unit fracture is a function of velocity and can be evaluated by means of velocity profile expression. **Equation 4.98** expresses the volumetric flow rate per unit fracture thickness:

$$\frac{q_z}{h_f} = \int_{-w/2}^{w/2} v_z dx \qquad \textbf{(Eq. 4.98)}$$

In **Equation 4.98;** q_z is volumetric flow rate, h_f is fracture thickness, w is fracture width and $\frac{\partial P}{dz}$ is pressure gradient **[Howard and Fast, 1970].**

Equation 4.97 is substituted to **Equation 4.98** to obtain **Equation 4.99:**

$$\frac{q_z}{h_f} = \int_{-w/2}^{w/2} \left(-\frac{1}{2\mu} \left[\left(\frac{w}{2} \right)^2 - x^2 \right] \frac{\partial P}{\partial z} \right) dx \qquad \textbf{(Eq. 4.99)}$$

Simplified form of **Equation 4.99** that is solved for volumetric flow rate is **Equation 4.100:**

$$q_z = \frac{h_f w^3}{12\mu} \frac{\partial P}{\partial z} \qquad \textbf{(Eq. 4.100)}$$

Equation 4.101 is Darcy's equation written in the differential form:

$$q = \frac{kA}{\mu} \frac{\partial P}{\partial z} \qquad \textbf{(Eq. 4.101)}$$

Equation 4.100 and **Equation 4.101** are combined to solve for permeability term that is expressed in terms of width. **Equation 4.102** is the form of cross sectional area that is expressed in terms of fracture thickness and fracture width:

$$A = h_f w \qquad \textbf{(Eq. 4.102)}$$

Equation 4.103, Equation 4.104 and **Equation 4.105** conclude the permeability term evaluation as shown below:

$$\frac{h_f w^3}{12} = kA = kh_f w \qquad \textbf{(Eq. 4.103)}$$

$$\frac{w^2}{12} = k \qquad \textbf{(Eq. 4.104)}$$

$$k = 5.45 \times 10^{7} w^{2} \qquad \textbf{(Eq. 4.105)}$$

Since 1 darcy is equal to 1.52973 x 10^{-9} in^2, necessary conversion can be reflected to **Equation 4.104**, where *w* is expressed in inches. **Equation 4.105** is the form of equation where permeability is expressed in darcies and width is expressed in inches.

4.6 Summary of the Procedure of the Approach

Stepwise analysis of the problem on which this thesis is based, is composed of three main steps.

The first step is deformation versus loading analysis and failure analysis. This step of the analysis is dependent on tarmat properties and dimensions. This step helps to determine failure envelope associated with the deformation versus loading analysis. Second step is the use of a conventional well test model or a numerical model. This model helps to study the relationship between pressure differential and time differential, for a range of various production rates. This study is dependent on reservoir properties and dimensions. The third and final step is fracture width estimation that would occur after geomechanical failure of tarmat and fracture permeability analysis that is dependent on fracture width. This step is dependent on tarmat properties and dimensions, water properties and reservoir production rate.

Chapter 5

Results and Discussions

The analysis this thesis is based on is composed of three main steps. Each step involves parametric analysis. First step deals with geomechanical failure of tarmat, second stage deals with expected pressure distribution during reservoir depletion and third step deals with fracture clearance and that would be created after geomechanical failure and permeability that would be established after fracture clearance occurs.

Having discussed the methodology in Chapter 5, this chapter presents the results and discussions of each stage separately followed with the suggested protocol to be followed in the complete analysis.

5.1 Failure Analysis

This stage of the analysis is a sensitivity analysis that investigates the behavior of tarmat as the overlying reservoir is being depleted. Reservoir depletion followed by increasing pressure differential acts as if there is an increasing loading is being applied to tarmat from the bottom. To model the behavior of tarmat under this circumstances, rectangular plate deformation model is used. In this model, deformation behavior of tarmat as loading on it increases is investigated until expected geomechanical failure occurs. Geomechanical failure of tarmat is characterized by maximum shear stress failure criterion. This analysis is made with two different assumptions, uniform loading

assumption and non-uniform loading assumption. These two protocols are discussed and compared in the following parts of this section.

5.1.1 Failure Analysis with Uniform Loading Assumption

In this part, failure analysis with uniform loading assumption, which means a loading assumption as if it has the same magnitude through the surface of tarmat, is discussed based on influential parameters.

Figure 5.1 shows deformation versus loading and the associated failure envelope with three different cases. In each of them, different tarmat thicknesses are used varying from *30 ft* to *100 ft*. Deformation versus loading behavior is investigated until the point where maximum shear stress failure criterion restricted this behavior and provided the conclusion of geomechanical failure. The curve combining the failure points for different thicknesses is referred as the failure envelope. Influential properties are Young's modulus of elasticity, Poisson's ratio, yield strength and lateral dimensions of tarmat. It should be noted that Young's modulus of elasticity is influential in deformational behavior determination. However, yield strength and Young's modulus of elasticity are specific for the material, and Young's modulus of elasticity has an indirect effect in determining the failure envelope. In **Figure 5.1** lateral dimensions are *750 ft* and Poisson's ratio is *0.30*. However Young's modulus of elasticity and yield strength are *3,000,000 psi* and *30,000 psi* in **Figure 5.1(a)**, *5,500,000 psi* and *50,000 psi* in **Figure 5.1(b)**, *8,000,000 psi* and *75,000 psi* in **Figure 5.1(c)**, respectively. **Figures 5.1(a)** through **5.1(c)** are drawn in the same scale to display explicitly the expected influences of main parameters in this

sensitivity analysis. Lateral dimensions and Poisson's ratio have been held constant in this part of the failure analysis since they are not dependent on elastic properties. Yield strength assumptions have been increased with Young's modulus of elasticity assumptions since they generally show a directional relationship in a specific material as their influences are discussed in following parts of the failure analysis.

In each of **Figure 5.1** a conclusion about thickness of tarmat is drawn. Thicker the tarmat, more pressure it requires encountering the geomechanical failure. However, thinner the tarmat, more deformation occurs until the observation of failure. As each of **Figure 5.1** are compared together the following can be deduced: As Young's modulus of elasticity and yield strength becomes higher, pressure required failing tarmat increases and deformation decreases slightly.

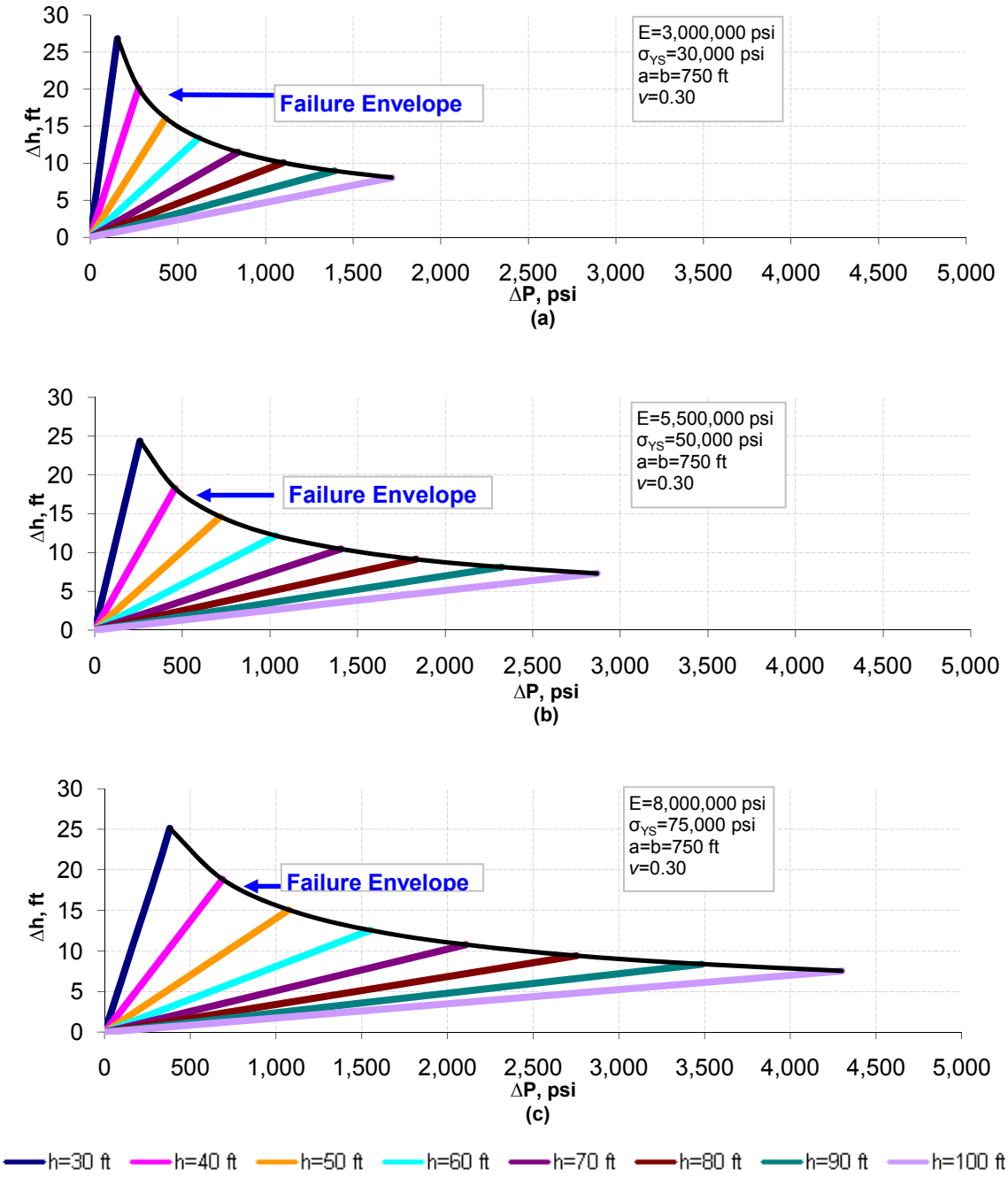

Figure 5.1: Deformation versus loading with associated failure envelope (a)E=3,000,000 psi, σ_{YS}=30,000 psi, a=b=750 ft, ν=0.30, (b)E=5,500,000 psi, σ_{YS}=50,000 psi, a=b=750 ft, ν=0.30, (c)E=8,000,000 psi, σ_{YS}=75,000 psi, a=b=750 ft, ν=0.30

Figure 5.2, Figure 5.3 and **Figure 5.4** display the magnitude and nature of the effects caused by the principal parameters of this analysis on failure pressure. Most influential parameters are lateral dimensions, yield strength and Poisson's ratio of tarmat. All of them also express direct proportion of tarmat thickness and magnitude of pressure required to geomechanically fail the tarmat, again. Each of **Figure 5.2, Figure 5.3** and **Figure 5.4** are drawn considering critical pressures and deformations that occur until critical pressure is reached.

Figure 5.2 presents the effect of lateral dimensions of tarmat on failure pressure due to various possible tarmat thicknesses. Corresponding reservoir drainage areas are expressed in **Figure 5.2.** Lateral dimensions are varied within a range of *500 ft* and *4,000 ft* while corresponding drainage areas vary between *5.75 acres* and *368 acres*. Young's modulus of elasticity, yield strength and Poisson's ratio are assigned to be *4,000,000 psi, 40,000 psi* and *0.30,* respectively. It is observed that in smaller drainage areas, more pressure differential is required to fail tarmat. This is due to the placement of artificial supports along the edges of the plate. The effects of these supports become less influential as the lateral extent of the system is increased.

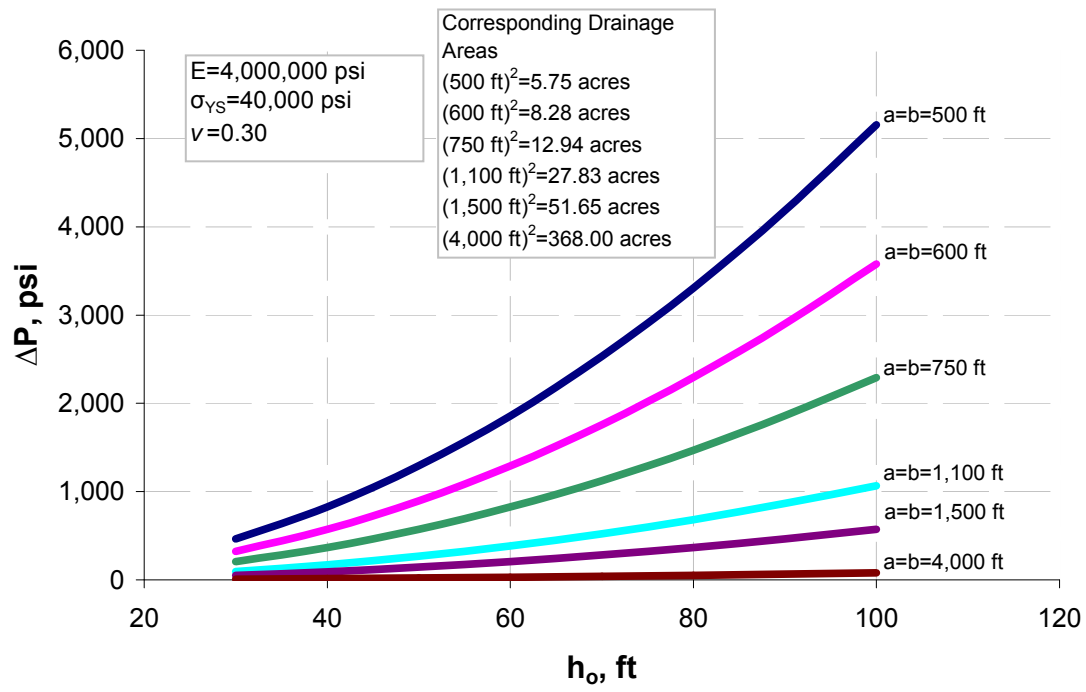

Figure 5.2: Loading versus thickness graph for various lateral dimensions (E=4,000,000 psi, σ_{YS}=40,000 psi, ν=0.30)

Figure 5.3 displays the effect of yield strength of tarmat on failure pressure due to various possible tarmat thicknesses. Yield strengths are varied within a range of *15,000 psi* and *100,000 psi*. Young's modulus of elasticity, Poisson's ratio and lateral dimensions are assigned to be *4,000,000 psi, 0.30* and *750 ft,* respectively. It is observed that tarmat having higher yield strengths, requires more pressure differential until geomechanical failure. This result is due to the fact that the maximum shear stress that occurs within the tarmat as loading increases is being compared with a higher yield strength value, letting pressure to increase for the material to reach that shear stress value.

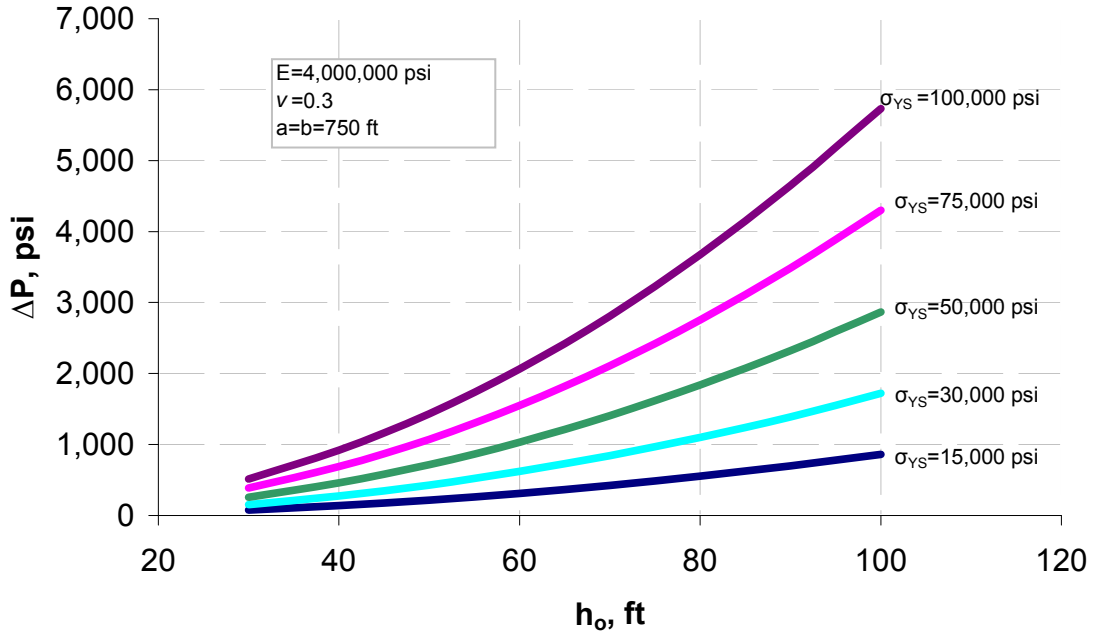

Figure 5.3: Loading versus thickness graph for various yield strengths (E=4,000,000 psi, ν =0.30, a=b=750 ft)

Figure 5.4 displays the effect of Poisson's ratio of tarmat on failure pressure due to various possible tarmat thicknesses. Poisson's ratios are varied within a range of *0.10* and *0.50*. Young's modulus of elasticity, yield strength and lateral dimensions are assigned to be *4,000,000 psi*, *40,000 psi* and *750 ft,* respectively. It is observed that tarmats with smaller Poisson's ratios, require more pressure differential until the failure point.

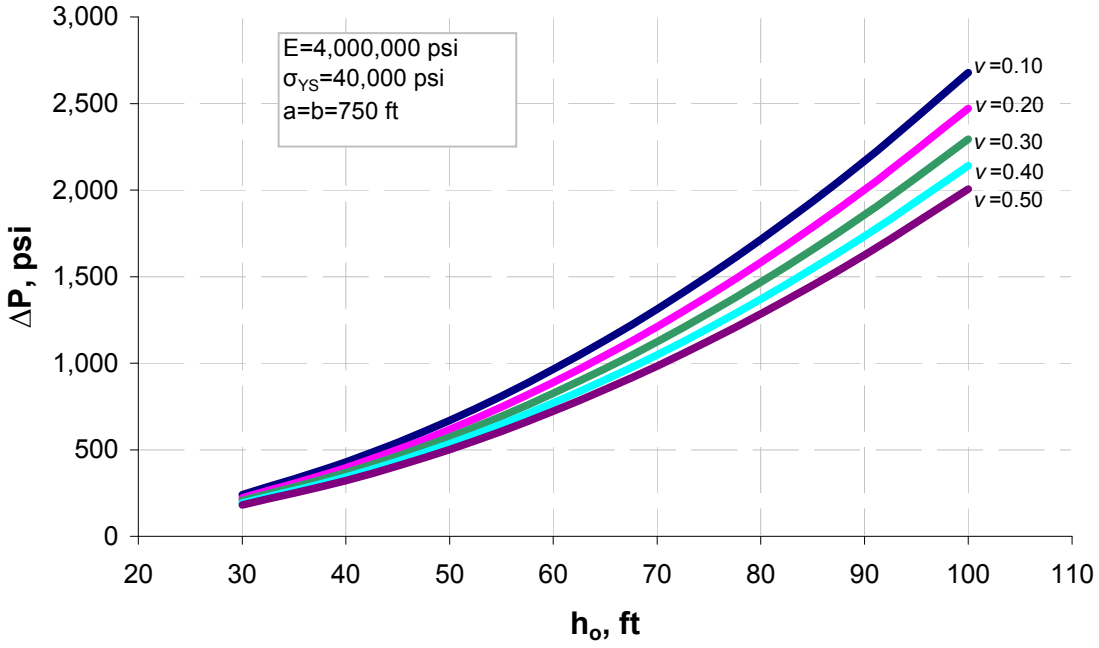

Figure 5.4: Loading versus thickness graph for various Poisson's ratios (E=4,000,000 psi, σ_{YS}=40,000 psi, a=b=750 ft)

5.1.2 Failure Analysis with Non-Uniform Loading Assumption

In this part, failure analysis with non-uniform loading assumption which is the most at the center and gets lower towards the edges is made. The results of this analysis and comments regarding the analysis itself and its comparison with uniform loading assumption is made in the following part of this section.

5.1.3 Comparison of Uniform and Non-Uniform Loading

In this part, failure analysis with uniform loading and failure analysis with non-uniform loading is compared.

Figure 5.5 displays a comparison between deformation versus loading and associated failure envelope of uniform loading **(a)** and non-uniform loading **(b).** For a tarmat with a certain thickness, lateral dimensions, Young's modulus of elasticity, Poisson's ratio and yield strength, more pressure differential is required to observe geomechanical failure in the case of non-uniform loading. More deformation would be observed in the case of a uniform loading. Difference in deformation amount is relatively small.

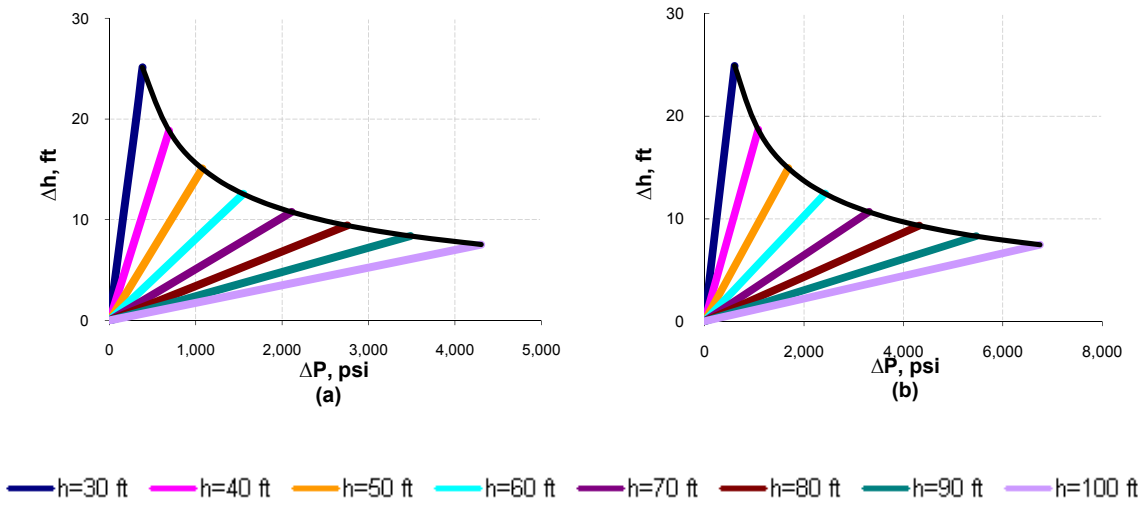

Figure 5.5: Comparison of deformation versus loading with associated failure envelope with uniform and non-uniform loading assumption (E=8,000,000 psi, σ_{YS}=75,000 psi, a=b=750 ft, ν=0.30)

Figure 5.6 displays a comparison between loading versus thickness for different lateral dimensions of tarmat in the cases of uniform loading **(a)** and non-uniform loading **(b).** For a tarmat of certain lateral dimensions, thickness, Young's modulus of elasticity, Poisson's ratio and yield strength, more pressure differential is required to observe geomechanical failure in the case of non-uniform loading.

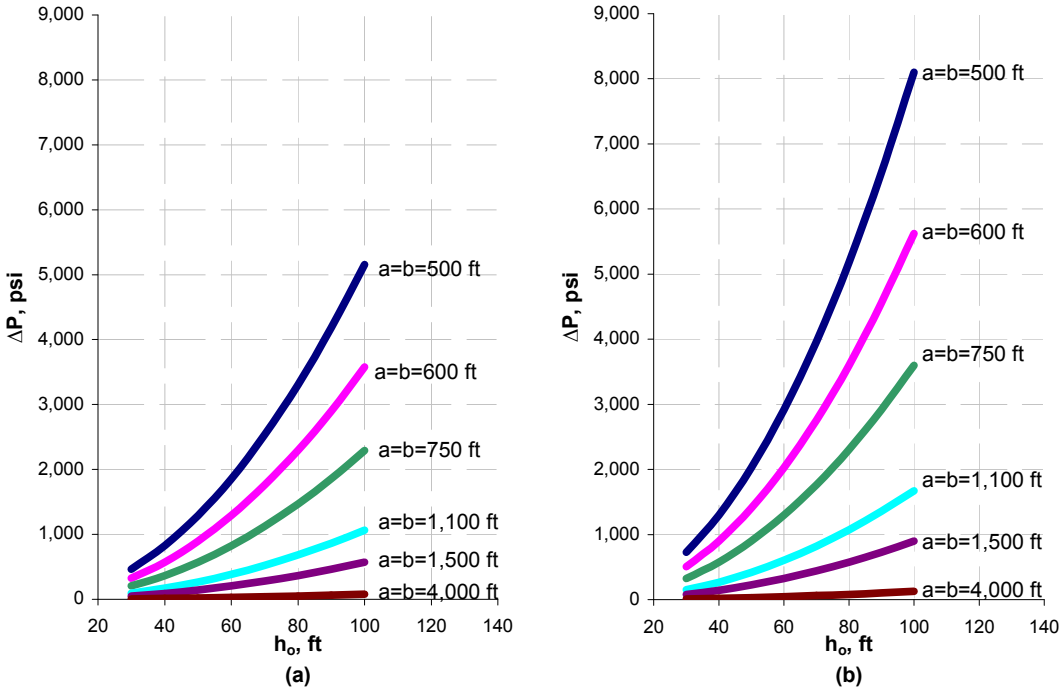

Figure 5.6: Comparison of loading versus thickness graphs for various lateral dimensions with uniform and non-uniform loading assumption

Figure 5.7 displays a comparison between loading versus thickness for different yield strengths of tarmat in the cases of uniform loading **(a)** and non-uniform loading **(b).** For a tarmat with a certain yield strength, lateral dimensions, thickness, Young's modulus of elasticity and Poisson's ratio, more pressure is required to observe geomechanical failure in the case of non-uniform loading.

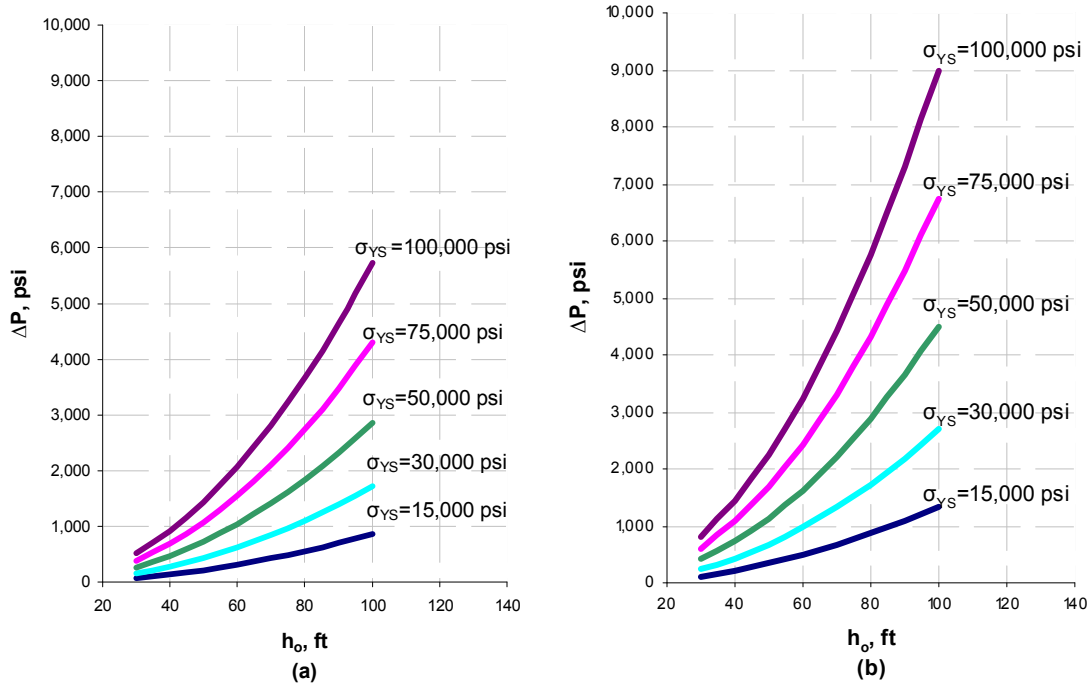

Figure 5.7: Comparison of loading versus thickness graph for various yield strengths with uniform and non-uniform loading assumption

Figure 5.8 displays a comparison between loading versus thickness for different Poisson's ratios of tarmat in the cases of uniform loading **(a)** and non-uniform loading **(b).** For a tarmat of certain Poisson's ratio, lateral dimensions, thickness, Young's modulus of elasticity, and yield strength, more pressure differential is required to observe geomechanical failure in the case of non-uniform loading.

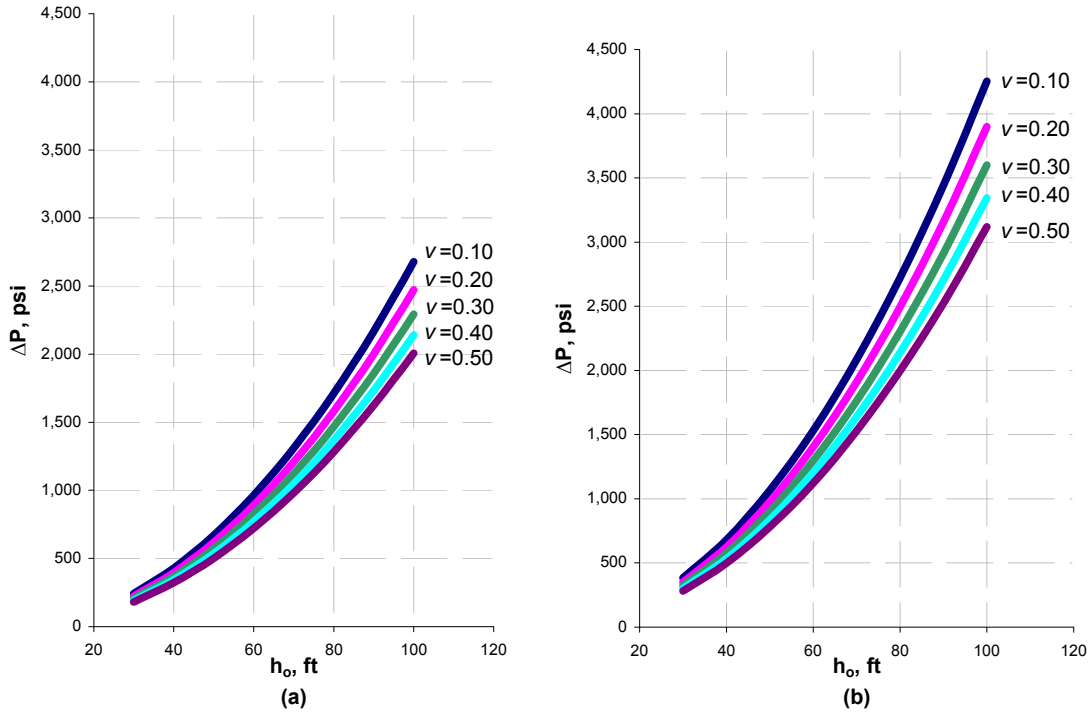

Figure 5.8: Comparison of loading versus thickness graph for various Poisson's ratios with uniform and non-uniform loading assumption

5.2 Pressure Transient Model

This stage of the analysis is dealing with reservoir depletion that occurs in the upper section of the composite system of interest. Conventional well test model is used to calculate the change of pressure in a single phase, square shaped reservoir, having a single well located at the center. By this model, pressure differential at a given time can be determined not only at the well point but also throughout the reservoir. However, main interest is the center, due to the fact that critical pressure that determines the instant of

failure occurs at the center. This study has been conducted for two different drainage area assumptions. In each case, production rate has been varied between *1,000 STB/d* and *10,000 STB/d*. Reservoir properties assigned in this analysis are given in **Table 5-1** below.

Table 5-1: Hydrocarbon Reservoir Properties

Property	Value	Unit
μ	0.72	cp
Ø	0.25	fraction
B	1.3	rb/stb
k	400	md
h	200	ft
c	0.0000015	psi^{-1}
r_w	0.5	ft
P_i	9,000	psi

Figure 5.9 provides a comparison of different drainage area assumptions while production rate influences on pressure versus time relationship can also be observed. **Figure 5.9 (a)** and **Figure 5.9 (b)** represent the analysis with drainage area assumption of 51.65 acres and **Figure 5.9 (c)** and **Figure 5.9 (d)** represent the analysis with drainage area assumption of 200 acres. These drainage areas represent lateral dimensions of *1,500 ft* and *2,952 ft* respectively. **Figure 5.9 (b)** and **Figure 5.9 (d)** show the zoomed portions of **Figure 5.9 (a)** and **Figure 5.9 (b)** respectively.

As production rate increases, a certain pressure differential is reached in a shorter period of time. This means that, as unloading occurs with a higher rate, critical pressures are reached faster. From **Figure 5.9** it can also be extracted that, similar production rates applied on reservoirs with different drainage areas result in different pressure versus time

behavior. For reservoirs with smaller drainage areas, it takes less time to reach a certain pressure differential than it does for those with larger drainage areas.

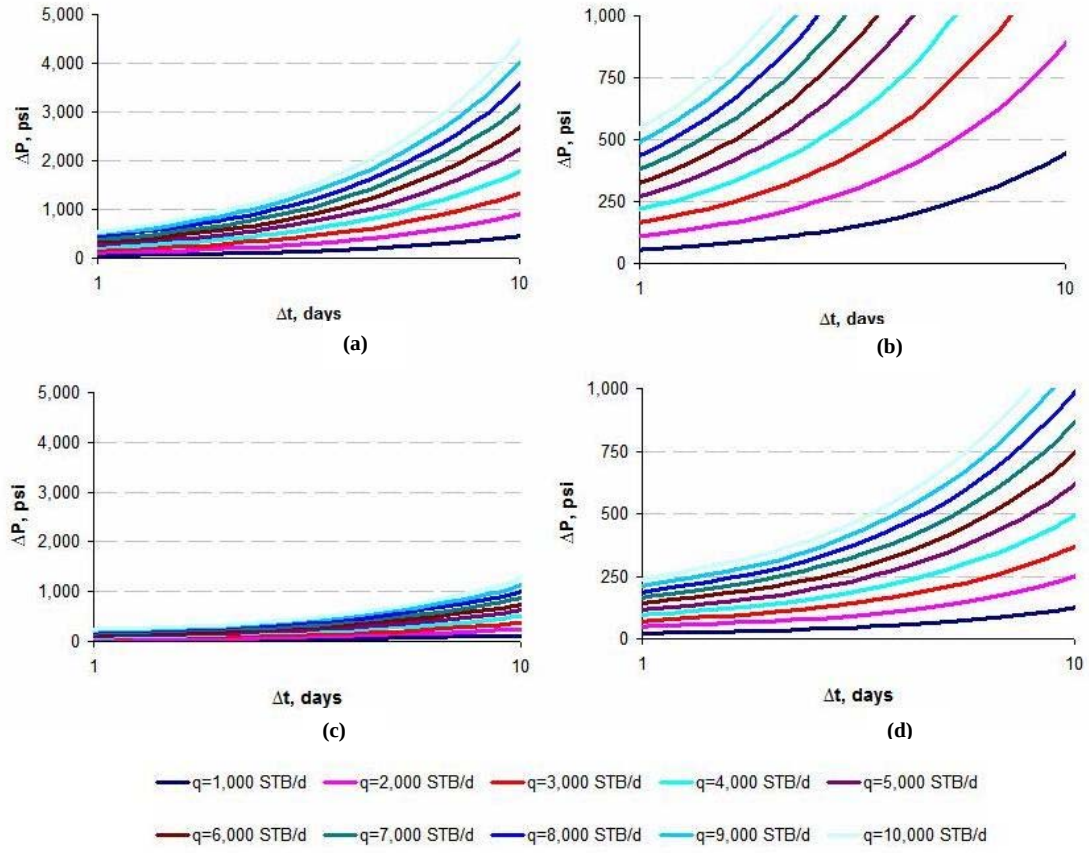

Figure 5.9: Pressure differential versus time differential graphs for various flow rates (a),(b): Cross sectional area=51.65 acres, (c),(d): Cross sectional area=200 acres

5.3 Characterization of the Formed Fractures

This stage of the analysis deals with the fracture width predictions. Two different hydraulic fracturing methodologies have been used to predict fracture width; PKN model and KGD model. Production rate from the reservoir above that would make a similar

effect as injection rate from the aquifer below has been used as an input flow rate. Range that has been used in the analysis with conventional well test model has been used. This production rate range is form *1,000 STB/d* to *10,000 STB/d*. This analysis that is relating production rate and width has been repeated for a possible range of tarmat thicknesses varying between *30 ft* and *100 ft*.

Figure 5.10 and **Figure 5.11** shows the relationship between fracture width and production rate as analyzed using the PKN model and KGD model respectively. Poisson's ratio has been assigned as *0.30* in both **Figure 5.10** and **Figure 5.11**. Young's modulus of elasticity has been assigned to be *3,000,000 psi* in **Figure 5.10 (a)** and **Figure 5.11 (a)** and *5,500,000 psi* in **Figure 5.10 (b)** and **Figure 5.11 (b)**. Fracture thickness, which corresponds to crack length through the tarmat layer is assigned to be *47.82 ft* as it corresponds to the assumed limitation that has been explained in Chapter 4. Fracture thickness is an influential input in KGD model, while it does not come into the picture in PKN model.

In both models, Young's modulus of elasticity is observed to be inversely proportional with fracture width. A system with a certain reservoir production rate and a certain tarmat thickness would encounter a wider width than another system having everything the same but the Young's modulus of elasticity higher. Apart form Young's modulus of elasticity, production rate is an influential parameter. A system with known properties encounter a wider crack width if the reservoir at the top of the system is being produced with a higher production rate. On the other hand thickness of tarmat is a significant parameter. Wider widths would be created in systems with thicker tarmat layers.

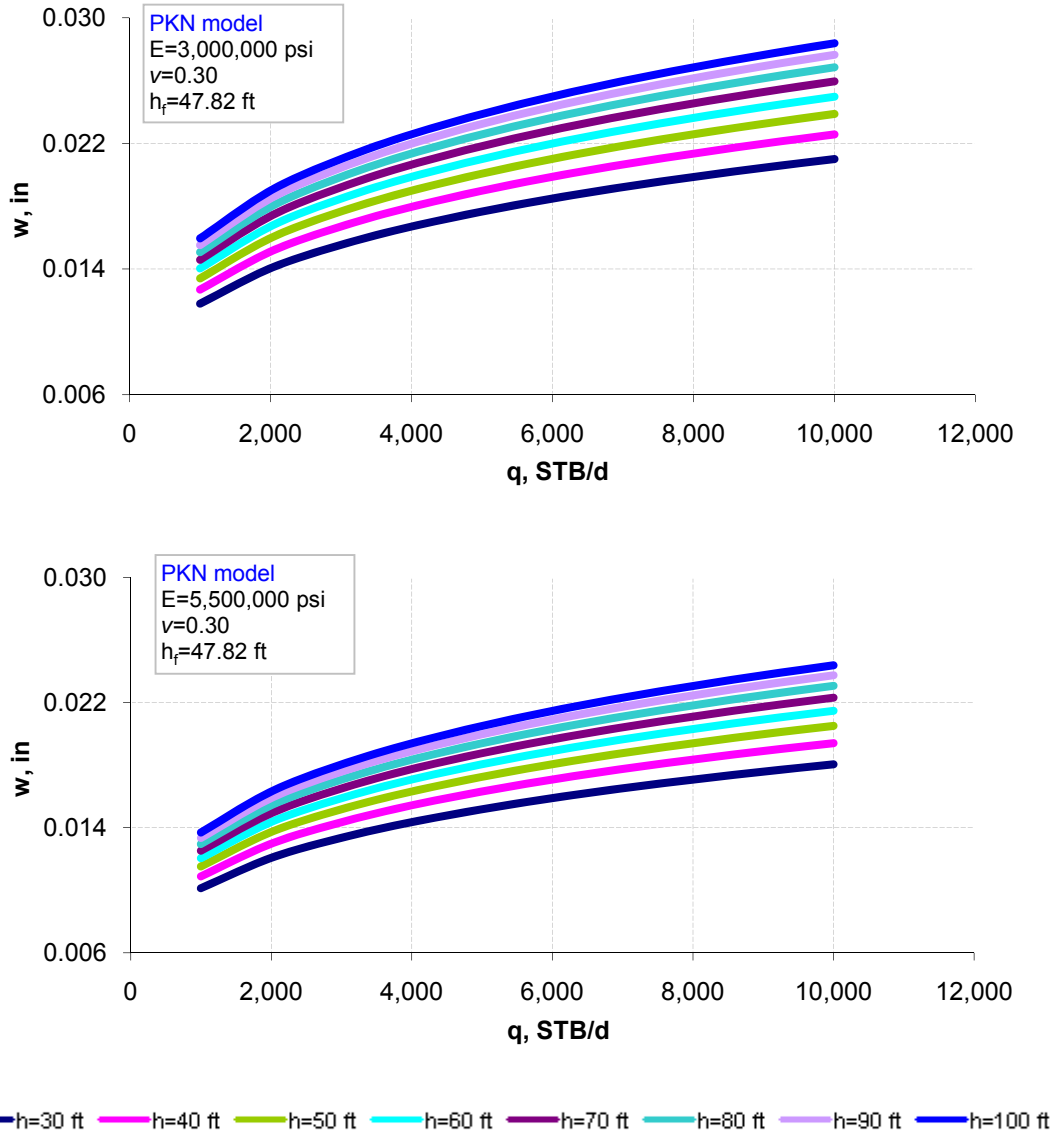

Figure 5.10: Width versus production rate graphs for various tarmat thicknesses (PKN model) (a)E= 3,000,000 psi, v=0.30, h_f=47.82 ft, (b) E=5,500,000 psi, v=0.30, h_f=47.82 ft

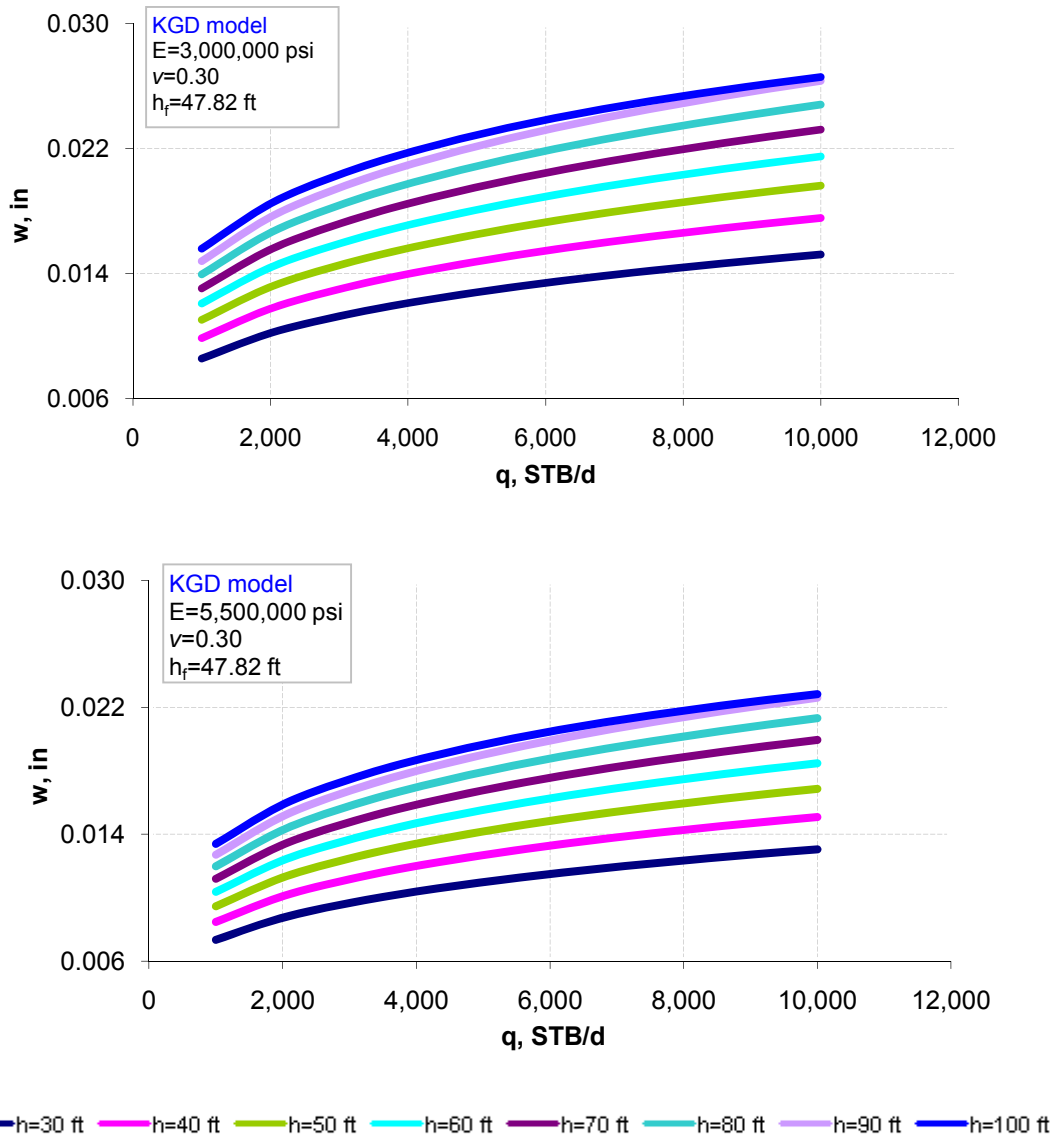

Figure 5.11: Width versus production rate graphs for various tarmat thicknesses (KGD model) (a)E= 3,000,000 psi, v=0.30, h_f=47.82 ft, (b) E=5,500,000 psi, v=0.30, h_f=47.82 ft

Apart from similar trends and relationships, there are differences and comparable predictions of PKN model and KGD model. PKN model predicts larger widths than KGD does. Difference in this prediction is largest in systems with high reservoir production

rates and thick tarmats. However, the difference becomes smaller in a system in which reservoir is being produced with a lower production rate and tarmat is thinner.

5.4 Permeability Analysis

Following graph, displayed in **Figure 5.12** shows a relationship between fracture permeability and fracture width. Equation 1 refers to the first method and equation 2 refers to the second method that are derived and explained in Chapter 4.

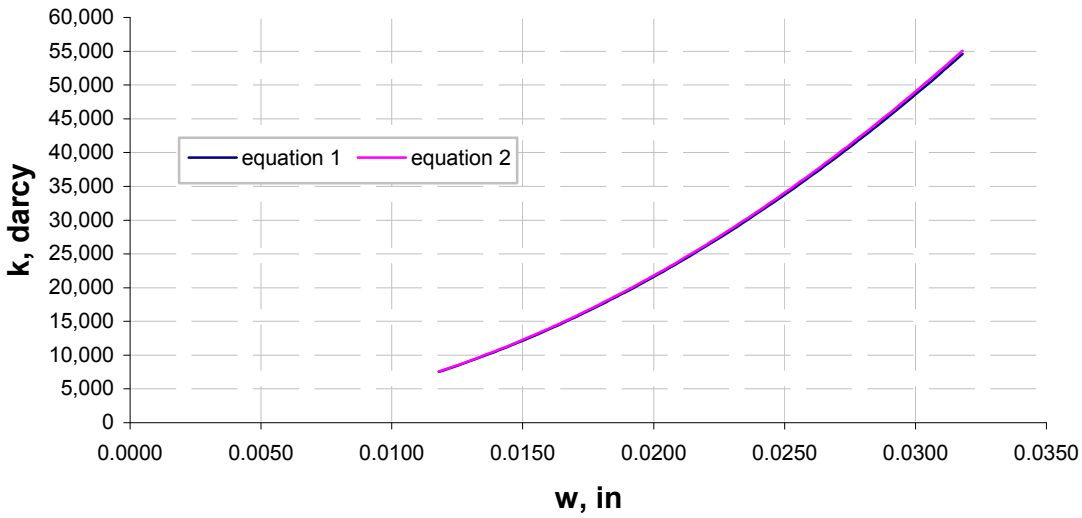

Figure 5.12: Fracture permeability versus fracture width

5.5 Suggested Computational Protocol

This part of the section presents the analysis of this study that attaches each separate step.

Suggested protocol is explained with selection of two different composite systems. In a certain stage of each system, two different assumptions are made and brought to the end of the analysis. This is explained in detail in following sections.

5.5.1 Case 1

Assigned properties of each layer of the composite system are given in **Table 5-2.**

Table 5-2: Assigned Properties of Composite System (Case 1)

	Property	Value	Unit
Hydrocarbon Reservoir		51.65	acres
	A	2,250,000	ft^2
	μ	0.72	cp
	Ø	0.25	fraction
	B	1.3	rb/stb
	k	400	md
	h	200	ft
	c	0.0000015	psi^{-1}
	r_w	0.5	ft
	P_i	9,000	psi
Tarmat	**v**	0.3	-
	E	8,000,000	psi
	a	1,500	ft
	b	1,500	ft
	h	80	ft
	σ_{YS}	30,000	psi
Fluid	**γ**	1	-
	μ	1	cp

First step of the protocol is the construction of deformation versus loading with associated failure envelope. This relation is dependent on Young's modulus of elasticity, yield strength, Poisson's ratio and lateral dimensions of the reservoir. **Figure 5.13** is the output of the study of this relation, for various inputs presented in the tarmat part of

Table 5-2. In **Figure 5.13**, determination of deformation and pressure magnitudes at the instant of failure have also been shown.

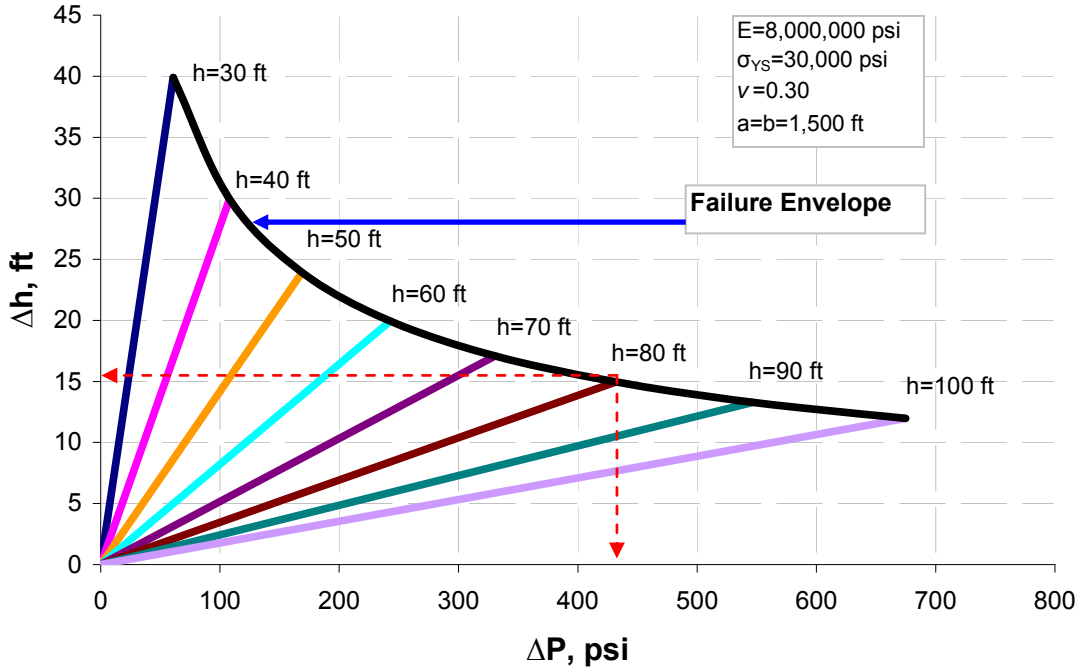

Figure 5.13: Deformation versus loading with associated failure envelope (E=8,000,000 psi, σ_{YS}=30,000 psi, a=b=1,500 ft, v=0.30)

As observed in **Figure 5.13**, by entering from the *80 ft* tarmat thickness line, magnitudes of deformation and pressure are found to be ***15 ft*** and ***432 psi***, respectively when failure takes place.

Second step involves the computation of the pressure differential with the help of the conventional well test model. Conventional well test model is used to obtain the relationship between pressure differential and time, for various flow rates within the chosen range. **Figure 5.14** is the output of the study of this relation, due to the inputs presented in hydrocarbon reservoir part of **Table 5-2.** Production rate selection or

producing time selection is required at this step. For this case, two different time selections have been made. First time selection is *3 days* and second time selection is *7 days*.

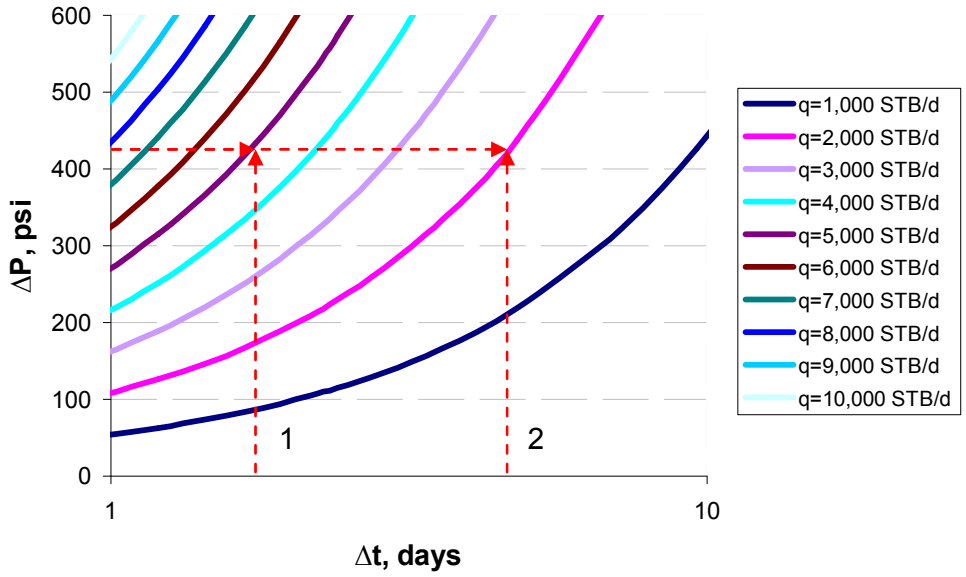

Figure 5.14: Pressure differential versus time differential graphs for various flow rates (Cross sectional area=51.65 acres)

As entered with the failure pressure of *432 psi* that is found in first step of the analysis, production rate for *3 day* time selection is ***5,000 STB/d*** and production rate for *7 day* time selection is ***2,000 STB/d***. This means that, if the hydrocarbon reservoir is to be produced at *5,000 STB/d,* tarmat with given material properties and dimensions would be exposed to its failure pressure in *3 days* and for the case *of 2,000 STB/d* production rate, failure pressure would be reached in *7 days*.

Following step is fracture width determination. Two different models, PKN model and KGD model are used in this third step. They are constructed for selected range of

production rates and tarmat thicknesses. Relation of width and production rate in **Figure 5.15** is the output, due to the inputs presented in tarmat part and fluid part of **Table 5-2.**

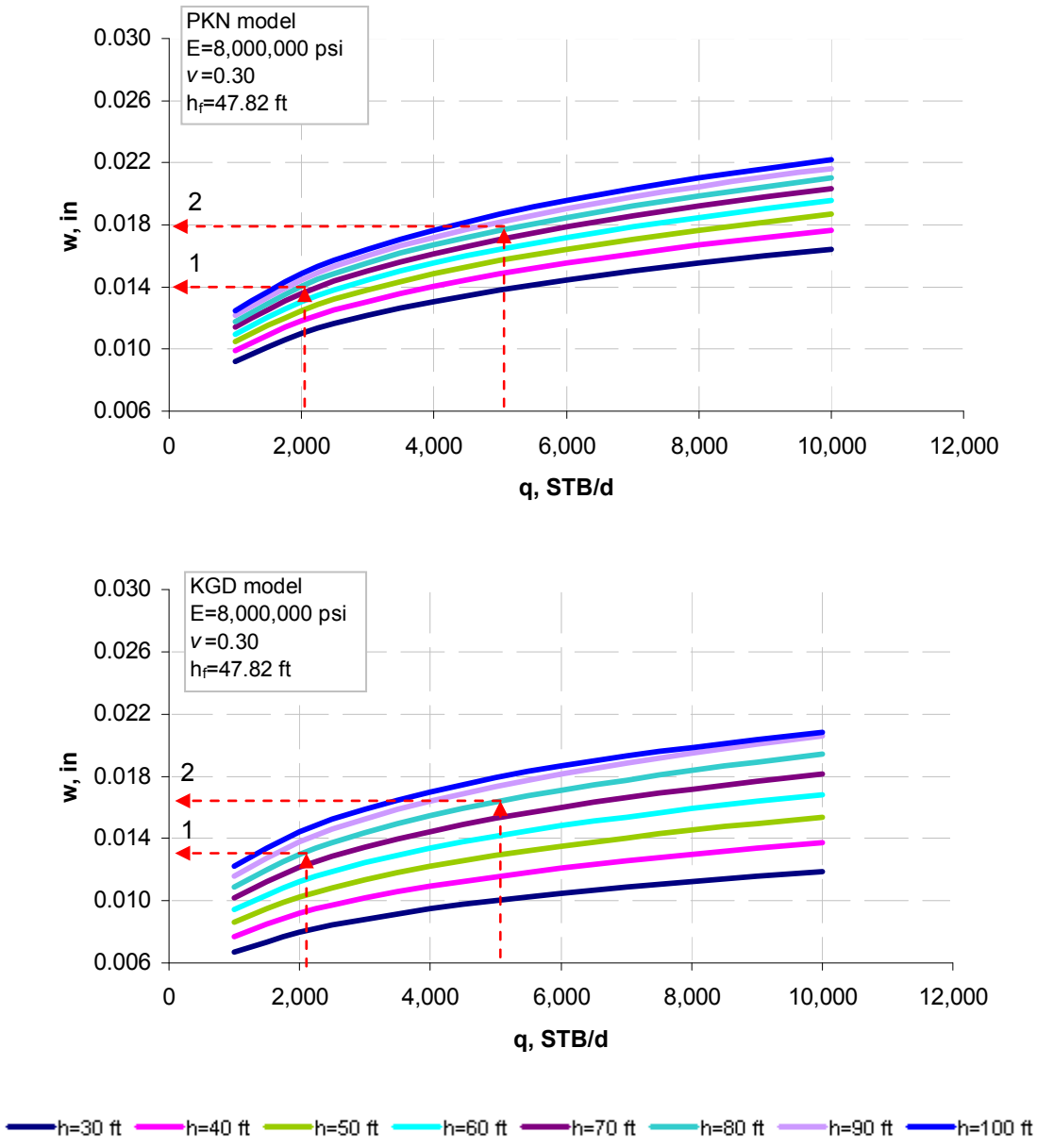

Figure 5.15: Width versus production rate graphs for various tarmat thicknesses (PKN and KGD model) (E=8,000,000 psi, v=0.30, h_f=47.82 ft)

Entering with production rates of *2,000 STB/d* and *5,000 STB/d*, thickness of *80 ft* is selected from family of thickness curves in both models. The y axis value of the two points on *80 ft* curve are the predictions for fracture widths. Fracture width due to *2,000 STB/d* production rate is predicted to be ***0.0140 in*** by PKN model and ***0.0130 in*** by KGD model. Similarly, a fracture width due to *5,000 STB/d* production rate is predicted to be ***0.0180 in*** by PKN model and ***0.0165 in*** by KGD model.

Final step of the analysis is determination of the permeability that would be established by the fracture widths that are created after geomechanical failure of tarmat. At this stage, relationship of permeability and fracture width that is studied for both rectangular fractures and hydraulic fractures is used. Average values of PKN model and KGD model predictions are found. These average widths are ***0.0135 in*** and ***0.0173 in*** for the first and second models, respectively.

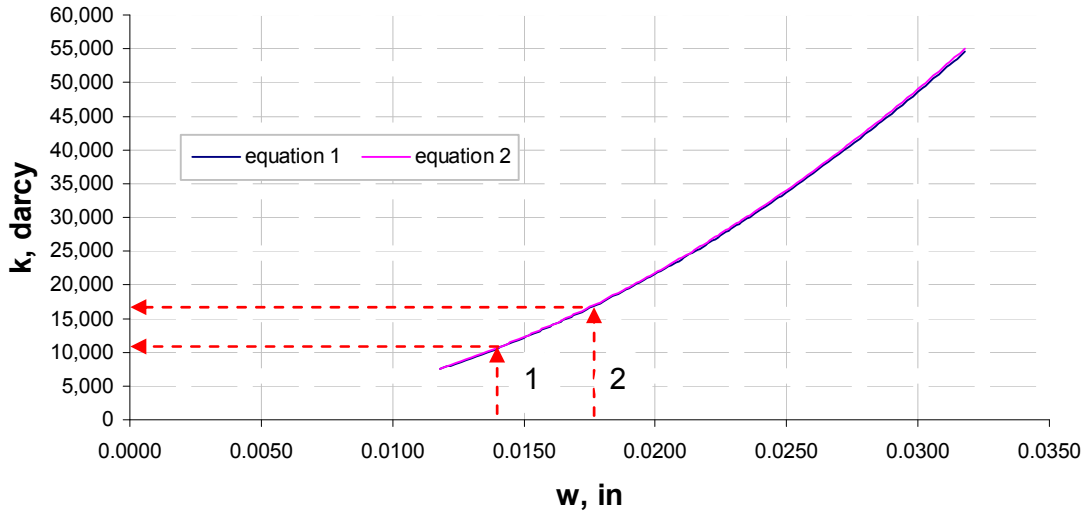

Figure 5.16: Fracture permeability versus fracture width

As entered with a fracture width of *0.0135 in*, permeability value is found to be ***10,500 darcy*** and as entered with a fracture width of *0.0173 in* permeability value is found to be ***16,000 darcy.***

This step is the end of this analysis associated with the given case. In summary, ***80 ft*** thick tarmat with given properties and dimensions would deform up to ***15 ft*** until its failure that would occur at ***432 psi*** of pressure differential. This pressure differential would be created in ***3 days*** at the well point with a production rate of ***5,000 STB/d*** and in ***7 days*** with a production rate of ***2,000 STB/d***. ***3 day*** long reservoir depletion would cause a fracture width of ***0.0173 in*** after the failure while ***7 day*** long reservoir depletion would cause a fracture with of ***0.0135 in***. ***0.0173 in*** wide fracture would establish a fracture permeability of ***16,000 darcy*** while ***0.0135 in*** wide fracture would establish a fracture permeability of ***10,500 darcy***. If failure pressure is reached in a shorter time with a higher production rate, fracture permeability is lower than a process with a longer time and lower production rate.

5.5.2 Case 2

Assigned properties of each layer of the composite system are given in **Table 5-2.**

Table 5-3: Assigned Properties of Composite System (Case 2)

	Property	Value	Unit
Hydrocarbon Reservoir		200	acres
	A	8,712,002	ft^2
	μ	0.72	cp
	Ø	0.25	fraction
	B	1.3	rb/stb
	k	400	md
	h	200	ft
	c	0.0000015	psi^{-1}
	r_w	0.5	ft
	P_i	9,000	psi
Tarmat	**v**	0.2	-
	E	5,000,000	psi
	a	2,952	ft
	b	2,952	ft
	h	90	ft
	σ_{YS}	20,000	psi
Fluid	γ	1	-
	μ	1	cp

The corresponding deformation versus loading with associated failure envelope is given in **Figure 5.17** due to the inputs presented in tarmat part of **Table 5-3.**

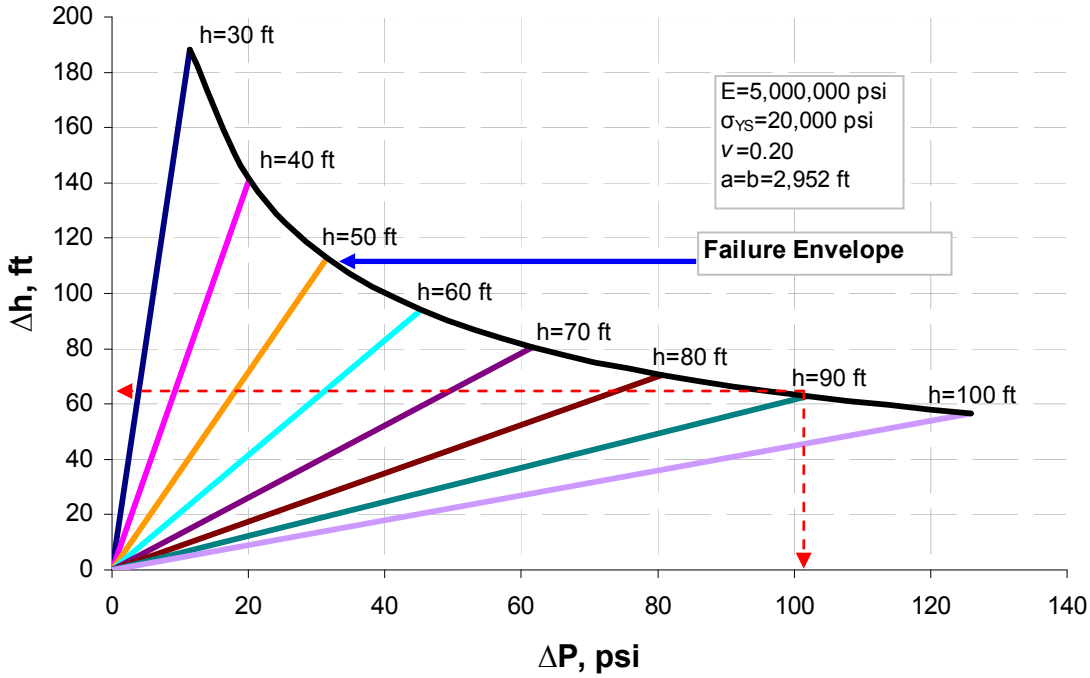

Figure 5.17: Deformation versus loading with associated failure envelope (E=5,000,000 psi, σ_{YS}=20,000 psi, a=b=2,952 ft, v=0.20)

As entered from *90 ft* tarmat thickness line, magnitudes of deformation and pressure are found to be ***63 ft*** and ***101 psi*** respectively.

Second step that is used for production rate prediction involves relevant conventional well test model study. **Figure 5.18** shows the relationship between pressure differential and time which is constructed due to the selected range of production rates and to the inputs presented in hydrocarbon reservoir part of **Table 5-3**. Producing time selections are made. First time selection is ***3 days*** and second time selection is ***9 days***, for this case.

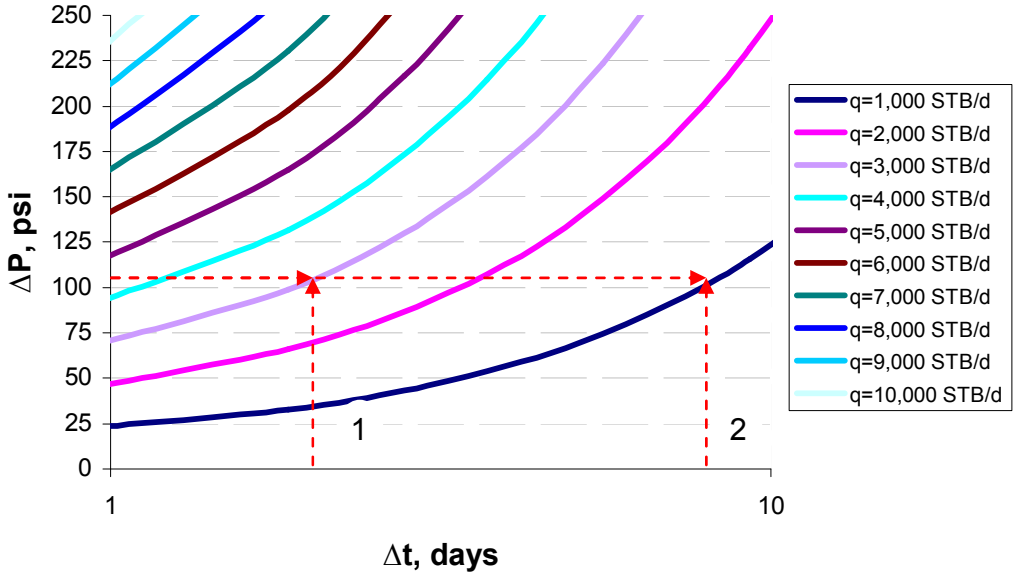

Figure 5.18: Pressure differential versus time differential graphs for various flow rates (Cross sectional area=200 acres)

As entered with the failure pressure of *101 psi* that is found in first step of the analysis, production rate for *3 day* time selection is ***3,000 STB/d*** and production rate for *9 day* time selection is ***1,000 STB/d***.

Following step is the fracture width determination. Two different models, PKN model and KGD model are used in this third step. They are constructed for selected range of production rates and tarmat thicknesses. Relation of width and production rate in **Figure 5.19** is the output, due to the inputs presented in tarmat part and fluid part of **Table 5-3.**

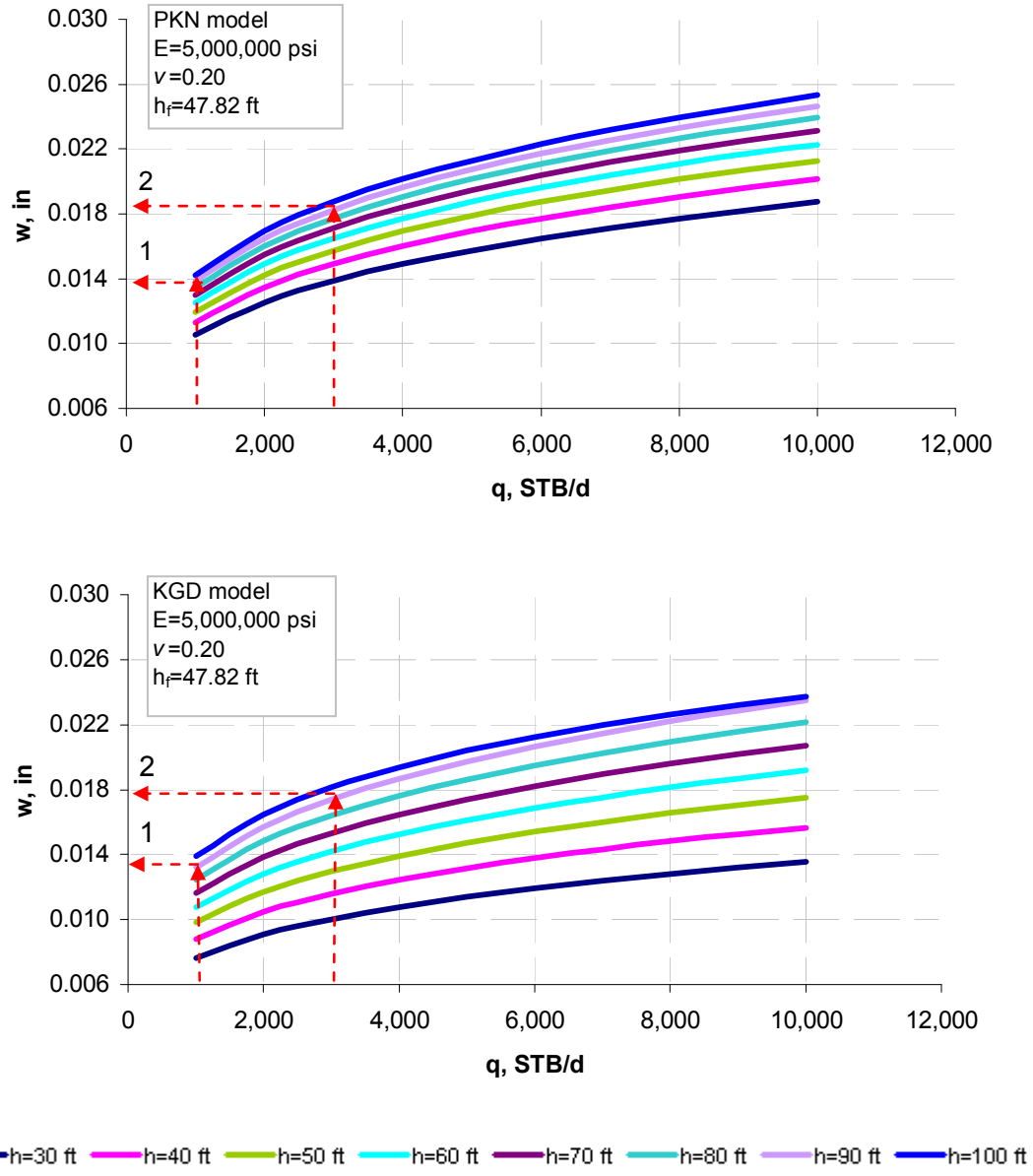

Figure 5.19: Width versus production rate graphs for various tarmat thicknesses (PKN and KGD model) (E=5,000,000 psi, v=0.20, h_f=47.82 ft)

Entering with production rates of *1,000 STB/d* and *3,000 STB/d*, thickness of *90 ft* is selected from family of thickness curves in both models. Fracture width for *1,000 STB/d* production rate is predicted to be ***0.0135 in*** by PKN model and ***0.0133 in*** by KGD

model. Fracture width of *3,000 STB/d* production rate is predicted to be ***0.0185 in*** by PKN model and ***0.0180 in*** by KGD model.

At this fourth and final step, relationship of permeability and fracture that has already been used in Case 1 and independent of material properties and dimensions have been used. Average values of PKN model and KGD model predictions are ***0.0134 in*** and ***0.0183 in*** for first selection and second selection, respectively.

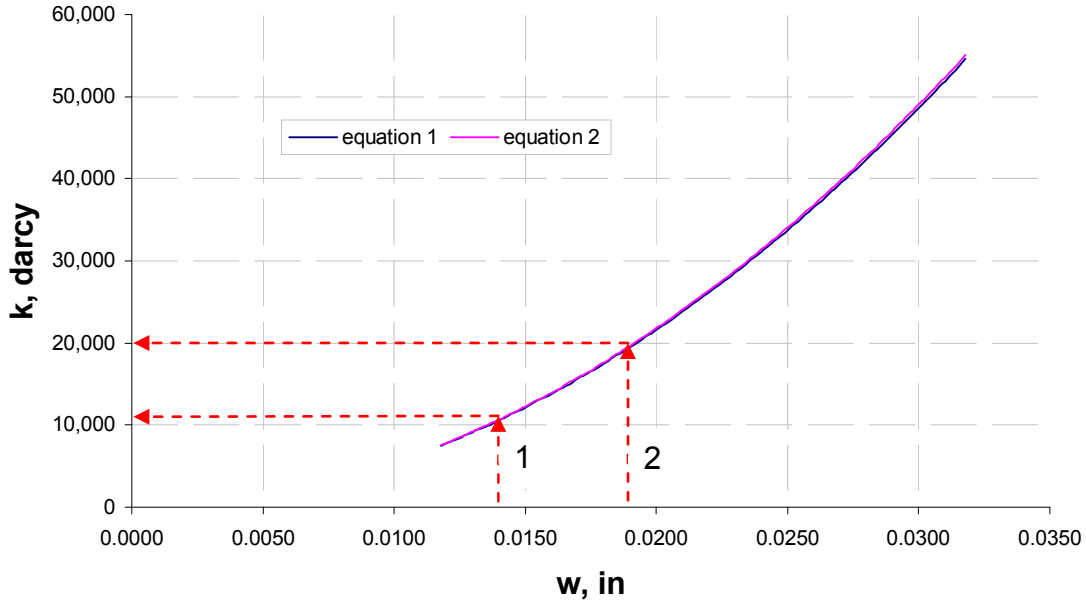

Figure 5.20: Fracture permeability versus fracture width

As entered with the width of *0.0134 in*, permeability value is found to be ***11,000 darcy*** and as entered with width of *0.0183 in* permeability value is found to be ***20,000 darcy.***

To summarize, ***90 ft*** thick tarmat with given properties and dimensions would deform up to ***63 ft*** until its failure that would occur at ***101 psi*** of pressure differential.

This pressure differential would be created in ***3 days*** with production rate of ***3,000 STB/d*** and in ***9 days*** with production rate of ***1,000 STB/d***. ***3 day*** long reservoir depletion would cause a fracture width of ***0.0183 in*** after the failure while ***9 day*** long reservoir depletion would cause a fracture with of ***0.0134 in***. ***0.0183 in*** wide fracture would establish a fracture permeability of ***20,000 darcy*** while ***0.0134 in*** wide fracture would establish a fracture permeability of ***11,000 darcy***.

5.6 Application of the Suggested Protocol to a Numerical Simulator

Suggested protocol for the problem of interest is summarized below:

1) *Input data:* These data are hydrocarbon reservoir properties, tarmat properties and fluid properties. Hydrocarbon reservoir properties are area, viscosity, porosity, formation volume factor, permeability, thickness, compressibility, wellbore radius and initial pressure. Tarmat properties are Poisson's ratio, Young's modulus of elasticity, lateral dimensions, thickness and yield strength. Fluid properties are specific gravity and viscosity.

2) *Failure analysis:* Deformation versus loading with associated failure envelope data can be embedded into a data matrix (in a table look-up form). This matrix would have deformation and corresponding loading values until failure points of possible tarmat thicknesses. Tarmat thickness from the input data can be used in the failure analysis to get two outputs; deformation and loading value at the failure point. Loading value would refer to the pressure differential value.

3) *Production rate and producing time analysis:* Pressure differential versus time differential graph for various flow rates can be embedded into another data matrix. This matrix would have pressure differential and corresponding time differential values for possible production rates. Output that comes from failure envelope analysis, pressure differential can be used in production rate analysis to have sets of differential time and production rates. In other words, this analysis would suggest production time choices, their corresponding production rates for reaching the previously obtained pressure differential. At this point, a certain production time which is coupled with a flow rate that is required in order to fail tarmat within selected time differential, should be selected.

4) *Fracture width analysis:* Fracture width versus production rate data for possible tarmat thicknesses can be embedded into two matrices: one relevant to the PKN model and the other relevant to the KGD model. Each of these matrices would have fracture width and corresponding production rate values for various tarmat thicknesses. Tarmat thickness from the input data and production rate from the output data set of the previous step can be used in fracture width analysis. Output of this part would be fracture width.

5) *Fracture permeability analysis:* Fracture permeability versus fracture width data can be embedded into the final matrix. This matrix would contain fracture permeability values that are corresponding to fracture widths. Fracture width that is output of the previous analysis can be used in this analysis to obtain relevant fracture permeability.

This aforementioned protocol may be incorporated into a dynamic numerical reservoir simulator. Before reservoir depletion starts, transmissibility values assigned

across the tarmat is zero. Pressure distributions at each iteration level of a certain time step are provided by the simulator. Maximum pressure differential created across the tarmat is compared with the failure pressure that is calculated from protocol described earlier. If failure pressure is larger than the maximum pressure differential that the most recent iteration within the current time step gives, a similar comparison is conducted within the next time step. This procedure may be repeated, until failure is concluded to have occurred. After this point, fracture width and fracture permeability values are calculated and transmissibility of the block hosting the fracture is updated accordingly. (It is important to note that obtained fracture permeability and width values are associated with the fracture).

Chapter 6

Summary, Conclusions and Recommended Future Work

6.1 Summary

In this work, tarmat deformation and failure behavior during depletion of a giant oil reservoir-aquifer system is studied. A mathematical model is developed for these kind of composite systems. Deformation response of tarmat to increasing pressure differential caused by continuous depletion of reservoir is studied and geomechanical failure that takes place is evaluated. Fracture that occurs after failure is characterized. Fracture permeability that is established due to the characterized fracture is studied. Plate theory, maximum shear stress failure criterion, conventional well test model, PKN model, KGD model, flow through fractures models have been combined in a suitable way. This sensitivity analysis is conducted with parameters of reservoir, rock and fluid properties. A protocol is proposed to find relationships and suggest designs in composite systems. The proposed methodology, predicts fracture width and fracture permeability that would be created in a system with a tarmat layer having a certain thickness and a reservoir being produced at a certain production rate and total depletion time.

Entire analysis is a procedure with three steps. First step is a sensitivity analysis that investigates deformation versus loading behavior and determines any failure envelope associated with deformation versus loading analysis. This analysis is a parametric study, based on plate theory that is forwarded to suitable case choice of

maximum shear stress failure criterion. Rectangular plate solution with simply supported boundary conditions is used for uniform and non-uniform loading configurations. Influential parameters at this stage are material properties and dimensions of tarmat. Material properties are, Young's Modulus of elasticity, Poisson's ratio and yield strength. Second step is the use of conventional well test model that helps to study the relationship between pressure differential and time differential. This step is not only dependent on reservoir properties and dimensions, but also production rate and selected well configuration. This step is conducted by choosing a certain range of production rates for different reservoir dimensions. Third step is the fracture width estimation that would occur after geomechanical failure of the tarmat and fracture permeability analysis that is dependent on estimated width of the fracture. This step is dependent on tarmat properties and dimensions, water properties and reservoir production rate. Influential tarmat properties are Young's Modulus of elasticity and Poisson's ratio and influential water properties are fluid viscosity and specific gravity. In order to find fracture permeability as a function of fracture width, two different approaches are used. They are; viscous flow of wetting fluids through smooth fractures of constant width and flow of hydraulically fracturing fluids through the induced fractures.

6.2 Conclusions

First, conclusions about deformation versus pressure differential and associated failure envelopes are presented, which are valid for both uniform and non-uniform loading configurations. Second, conclusions reached from comparison of uniform and

non-uniform loading configurations are provided. Then, conclusions drawn from well test analysis are presented followed by fracture width prediction conclusions. Finally, conclusions related to fracture permeability analysis are given.

Within the bounds of the followed procedure; following conclusions are drawn:

1. As thickness of tarmat increases, total deformation that occurs until the failure point decreases.

2. As thickness of tarmat increases, pressure differential that is required to geomechanically fail tarmat increases.

3. As Young's modulus of elasticity and yield strength of tarmat increase (which are in direct proportion with each other), pressure differential that is required to geomechanically fail tarmat increases.

4. As Young's modulus of elasticity and yield strength of tarmat increases, deformation amount that occurs until geomechanical failure of tarmat decreases. However, decrease/increase in deformation is not significant.

5. As tarmat area, or its lateral dimensions increase, pressure differential that is required to geomechanically fail tarmat decreases.

6. As yield strength of tarmat increases, pressure differential that is required to geomechanically fail tarmat increases.

7. As Poisson's ratio of tarmat increases, pressure differential that is required to geomechanically fail tarmat decreases.

8. A case of non-uniform loading requires more pressure until geomechanical failure, than a similar case with uniform loading configuration.

9. A case of non-uniform loading experiences less deformation until geomechanical failure, than a similar case with uniform loading configuration.

10. The PKN model predicts larger fracture widths than KGD model does. This difference is most obvious in the cases of thick tarmats and high production rates.

11. Each model predicts wider cracks in the cases of higher reservoir production rates.

12. Each model predicts wider cracks in the cases of thicker tarmats.

6.3 Recommended Future Work

Within the overall scope of this thesis, there are some areas that may be improved and brought further. The protocol suggested in this thesis provides a path to study more complex problems or similar problems with a more detailed approach. Recommendations along these lines are provided below:

1. In order to increase the universality of the solutions presented, it is suggested to express all of the relevant charts in a dimensionless form.

2. Suggested protocol that can be incorporated with a numerical simulator, can be evaluated for further analysis of the composite system. After finding the iteration level in the time step whose pressure distribution corresponds to the failure pressure of suggested protocol, fracture permeability would be found after finding fracture width. This permeability is associated only with the opening that has been created through the tarmat. Fracture permeability needs to be converted to an overall tarmat permeability for the tarmat block(s) containing the fracture.

3. Experimental data would help to evaluate the accuracy of the approach proposed. Triaxial test is suggested to be made with the rock specimens of interest, in order find their strengths. Peak load and the deformation of the specimen at the peak load for representative rock samples would help to select a curve from family of curves that have been used in failure analysis part of this work.

4. In this analysis, each step focuses on the behavior of a certain layer. For example, failure analysis is done by approaching tarmat as a rectangular plate. This analysis provides an estimation on tarmat failure behavior, however, entire composite system can be analyzed with the consideration of each layer being attached to each other and would behave together. Fracture, which is expected to initiate on the upper surface of the tarmat, is recommended to be analyzed in detail. Fracture penetration level through the tarmat can be analyzed in detail as a function of time without assuming that it would penetrate through the entire thickness of the tarmat.

References

Bickford, W.B., 1998, Advanced Mechanics of Materials: Addison-Wesley, Menlo Park, California

Boresi, A. P., Schmidt R. J., 2003, Advanced Mechanics of Materials, John Wiley and Sons, United States

Craft, B. C., Hawkins, M. F., 1959, Applied Petroleum Reservoir Engineering: Prentice Hall, New Jersey

Earlougher, R. C., Jr., 1977, Advances in Well Test Analysis: Society Petroleum Engineers of AIME, Dallas

Earlougher, R. C., Jr., Ramey, H. J., Jr., Miller, F. G., Mueller, T. D., 1968, Pressure Distributions in Rectangular Reservoirs: J. Pet. Tech., Trans., AIME, 243.

Economides, M. J., 1992, A Practical Companion to Reservoir Simulation: Elsevier Science, Netherlands

Economides, M. J., Watters, L. T., Dunn-Norman, S., 1998, Petroleum Well Construction: John Wiley and Sons, Chichester

Fjaher E., Holt, R.M., Horsrud, P., Raaen, A.M., Risnes R., 1992, Petroleum Related Rock Mechanics: Elsevier Science, New York

Gere, J. M., 2001, Mechanics of Materials: Brooks/Cole, United States

Goodman, R.E., 1989, Introduction to Rock Mechanics, John Wiley and Sons, Toronto

Howard, G. C., Fast C. R., 1970, Hydraulic Fracturing: Society Petroleum Engineers of AIME, Dallas

Lee, J., 1982, Well Testing: Society Petroleum Engineers of AIME, United States

Lianyang, Z. 2005, Engineering Properties of Rocks: Elsevier, United Kingdom

Nehring, R., 1978, Giant Oil Fields and World Oil Sources: The Rand Corporation, Santa Monica

Timoshenko, S., Woinowski-Krieger, S., 1959, Theory of Plates and Shells: McGraw Hill, United States

Toulokian, Y. S., Judd, W. R., Roy, R.F., 1981, Physical Properties of Rocks and Minerals: McGraw Hill, United States

Whittaker, B. N., Singh R.N., Sun, G., 1992, Rock Fracture Mechanics, Principles, Design and Applications: Elsevier Science, Amsterdam

Yew, C. H., 1997, Mechanics of Hydraulic Fracturing: Gulf Publishing Company, Houston